Carbon Cluster Formation during Thermal Decomposition of Octahydro-1,3,5,7-tetranitro-1,3,5,7-tetrazocine and 1,3,5-Triamino-2,4,6-trinitrobenzene High Explosives from ReaxFF Reactive Molecular Dynamics Simulations

Luzheng Zhang,[†] Sergey V. Zybin, Adri C. T. van Duin,[‡] Siddharth Dasgupta, and William A. Goddard III*

Materials & Process Simulation Center, California Institute of Technology, Pasadena, California 91125

Edward M. Kober

Theoretical Division, Los Alamos National Laboratory, Los Alamos, New Mexico 87545

Received: February 13, 2009; Revised Manuscript Received: June 23, 2009

We report molecular dynamics (MD) simulations using the first-principles-based ReaxFF reactive force field to study the thermal decomposition of 1,3,5-triamino-2,4,6-trinitrobenzene (TATB) and octahydro-1,3,5,7-tetranitro-1,3,5,7-tetrazocine (HMX) at various densities and temperatures. TATB is known to produce a large amount (15−30%) of high-molecular-weight carbon clusters, whereas detonation of nitramines such as HMX and RDX (1,3,5-trinitroperhydro-1,3,5-triazine) generate predominantly low-molecular-weight products. In agreement with experimental observation, these simulations predict that TATB decomposition quickly (by 30 ps) initiates the formation of large carbonaceous clusters (more than 4000 amu, or ∼15−30% of the total system mass), and HMX decomposition leads almost exclusively to small-molecule products. We find that HMX decomposes readily on this time scale at lower temperatures, for which the decomposition rate of TATB is about an order of magnitude slower. Analyzing the ReaxFF MD results leads to the detailed atomistic structure of this carbon-rich phase of TATB and allows characterization of the kinetics and chemistry related to this phase and their dependence on system density and temperature. The carbon-rich phase formed from TATB contains mainly polyaromatic rings with large oxygen content, leading to graphitic regions. We use these results to describe the initial reaction steps of thermal decomposition of HMX and TATB in terms of the rates for forming primary and secondary products, allowing comparison to experimentally derived models. These studies show that MD using the ReaxFF reactive force field provides detailed atomistic information that explains such macroscopic observations as the dramatic difference in carbon cluster formation between TATB and HMX. This shows that ReaxFF MD captures the fundamental differences in the mechanisms of such systems and illustrates how the ReaxFF may be applied to model complex chemical phenomena in energetic materials. The studies here illustrate this for modestly sized systems and modest periods; however, ReaxFF calculations of reactive processes have already been reported on systems with ∼10^6 atoms. Thus, with suitable computational facilities, one can study the atomistic level chemical processes in complex systems under extreme conditions.

1. Introduction

The advances in state-selected experimental technology and accurate first principles quantum mechanics over the last 20 years have led to a detailed understanding of the reaction mechanisms and kinetics for a number of gas-phase bimolecular and unimolecular reactions. However, little progress has been made in elucidating such atomistic detail about the very complex phenomena occurring in condensed-phase chemistry under the extreme conditions of high temperature and high pressure, particularly when these quantities fluctuate rapidly, as in shock-induced decomposition. Indeed, the complexity of the reactions in such systems with numerous intermediates interacting simultaneously might appear to preclude ever obtaining a detailed atomistic understanding of the chemical processes because of the need to examine the reaction surfaces of many thousands of atoms for many nanoseconds or longer.

To enable the computational study of such large systems for such long periods, we developed the ReaxFF reactive force field that retains nearly the accuracy of quantum mechanics (QM) but allows molecular dynamics (MD) for computational costs nearly as low as for simple force fields. ReaxFF reproduces the quantum chemical data for an extended set of unimolecular reaction pathways, including ground states, reaction intermediates, and transition states. Applications using ReaxFF for studying reactive processes have been reported for many systems, including organic reactions;[1] reactions of energetic materials (EMs), such as RDX and HMX under extreme conditions;[2,3] decomposition of improvised explosive devices, such as TATP;[4] thermal decomposition of polymers, such as silicones;[5] tribology of metal−metal oxide interfaces;[6] catalytic formation of carbon nanotubes;[7] storage of H_2 in Mg nanoclusters;[8] Si/SiO_2 oxidation;[9] crack propagation in silicon crystals;[10]

* Corresponding author. Phone: (626) 395-2731. Fax: (626) 585-0918. E-mail: wag@wag.caltech.edu.

[†] Current address: The Petroleum Recovery Research Center, New Mexico Tech, Socorro, New Mexico 87801.

[‡] Current address: Department of Mechanical and Nuclear Engineering, Pennsylvania State University, University Park, Pennsylvania 16802.

10.1021/jp901353a CCC: $40.75
Published on Web 10/01/2009

dissociation of H_2 on Pt surfaces;[11] propene-selective oxidation over $BiMoO_x$ heterogeneous catalysts;[12] and catalysis and ion transport in fuel cells.[13]

We consider that these extensive applications validate the overall quality of ReaxFF to describe the reactive potential surfaces for complex systems. Most valuable now will be the application of ReaxFF for elucidating reactive processes under extreme conditions at subnanosecond scale, where it is been difficult to obtain experimental characterizations. In particular, we consider here two energetic substances for which the detonation phenomena are known to result in dramatically different product distributions:

(1) TATB (1,3,5-triamino-2,4,6-trinitrobenzene or $C_6H_6N_6O_6$), an aromatic benzene-based high explosive (HE) known to produce large amounts (15−30%) of high-molecular-weight carbon clusters (soot), and

(2) HMX (octahydro-1,3,5,7-tetranitro-1,3,5,7-tetrazocine or $C_4H_8N_8O_8$), an example of a nitramine-based HE whose detonation generates predominantly low-molecular-weight gaseous products and no soot.

These HMX and TATB energetic materials are commonly used in various propellants. The ReaxFF MD simulations predict that by 30 ps, TATB decomposition initiates the formation of large carbonaceous clusters (∼15−30% of the total system mass is in clusters with more than 4000 amu), whereas HMX decomposition leads almost exclusively to small-molecule products. This agrees well with experimental observation, demonstrating that ReaxFF MD captures the fundamental differences in the mechanisms of such systems. Our analysis illustrates how ReaxFF may be used to characterize complex chemical phenomena.

The studies presented here include only modestly sized systems and modest time periods. However, ReaxFF calculations of reactive processes have already been proved practical for large systems using parallel computers; for example, $\sim 2 \times 10^6$ atoms for shock decomposition of RDX.[42,43] Thus, with suitable computational facilities, one can consider studies of chemical processes at the atomistic level for complex systems under extreme conditions.

The chemistry and physics of the formation and evolution of condensed carbon phases are very important aspects of the detonation of nitroaromatic explosives. The discovery of the synthesis of ultradispersed diamond (UDD) by detonation in hermetic tanks[14−19] has initiated numerous experimental studies to understand its kinetics and influence on various detonation phenomena, such as the detonation build-up of carbon-rich explosives. These experimental studies show that such explosives can produce a high yield of soot (up to 20−30%) containing micrometer-scale carbon clusters.[20−27] Kinetic mechanisms have been proposed to characterize the formation of such clusters in detonation waves and their effect on the decomposition chemistry.[28−32] However, because of the extremely high temperature, high pressure, and the dramatic variations of these quantities over very short time and length scales, it has not been possible to measure directly the compositions and phase evolution of the reaction products as the detonation wave passes through the material. Thus, available experimental information is limited to analysis of the final solid carbon residue (soot) after the expansion and cooling of the detonation products has been completed. Consequently, the experiments have not provided the data to disentangle the various fundamental steps at the early stages of HE decomposition that ultimately determine the final product distributions.

Determining the chemical or atomic mechanisms underlying the formation of primary products and aggregates at the initial stages of detonation and their evolution after the expansion and cooling should explain the differential kinetics of carbon condensation between HMX and TATB. In addition, it should improve equations of state used in the continuum mechanics simulations of such materials under reaction conditions. Developing such detailed chemical kinetics of thermal decomposition reactions should assist in the understanding of the relation of structure in determining the sensitivity of solid explosives to mechanical or thermal shocks, evolution of hot spots, and formation of the reaction zone in the detonation wave. Such thermal and chemical kinetic data is essential to the development of continuum decomposition models to predict the critical conditions for ignition and energy release in hot spots.

QM studies have been most useful for understanding unimolecular and simple bimolecular processes of small molecules (<50 atoms), but QM is not practical for following the molecular dynamics (MD) for the reaction pathways for systems containing 10 000 to 1 000 000 atoms over the periods of many nanoseconds that are required to describe the reactions involved in condensed-phase explosive processes.

In contrast, ReaxFF reaction dynamics is practical for studying high-temperature MD (ReaxFF-MD) of realistic, chemically reacting EM systems and can provide detailed information on the atomistic mechanisms of the chemical reactions taking place during the decomposition and subsequent reactions of EM under extreme conditions. Our goal is to elucidate the dominant reaction pathways as EMs decompose and to describe the events in this reaction mixture as it evolves to form intermediates that react with each other and with reactant to form eventually the final products observed experimentally. In this work, we focus on thermal decomposition of two typical condensed-phase energetic materials, HMX and TATB, and examine the kinetics for formation of carbonaceous clusters in the condensed phase ($C_6H_6N_6O_6$).

We interpret our results in terms of the evolution of primary and secondary reaction products plus the kinetics for forming carbonaceous clusters during the condensed-phase decomposition of pure HMX and TATB crystals. This provides an atomistic level understanding of many complex physiochemical processes under the extreme conditions typical for detonation.

2. Modeling Approach

2.1. ReaxFF Reactive Force Field. Critical aspects of ReaxFF are the following:[1,7,9]

(1) The instantaneous charge on each atom is determined by the electrostatic field due to all other charges in the system plus a simple, second-order description of the dependence of the internal energy of the atom on charge (expressed in terms of electronegativity and hardness). Here, the interaction between two charges is written as a shielded Coulomb potential so that it is well-behaved, even between bonded atoms. Here, we use the EEM variant[44,45] of the charge equilibration approach.[46] This Coulombic energy (E_{Coulomb}) acts among all atoms, including bonded ones (not nearest neighbor cutoffs).

(2) The instantaneous valence force and interaction energy between two atoms is determined by the instantaneous bond order, which in turn is determined by the instantaneous bond distance. These relationships are continuous and monotonic with the parameters determined by multiple QM calculations involving each type of bond-breaking processes. The bond orders are updated every MD step, thus allowing the ReaxFF to recognize new bonds and to break existing bonds between the atoms of reacting molecules.

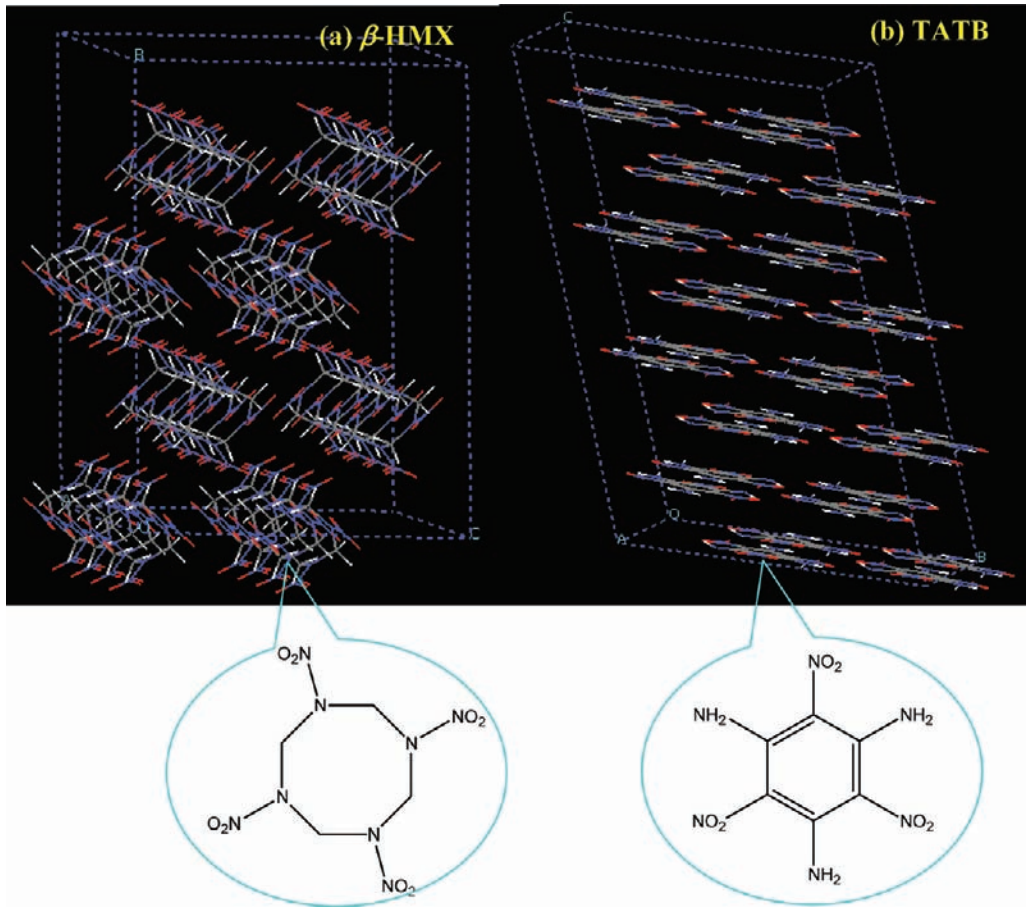

Figure 1. Molecular and crystal structures of (a) β-phase of HMX and (b) TATB within the simulation supercells.

(3) Other valence interactions are written in terms of the bond order so that they all go smoothly to zero as bonds dissociate. This includes bond (E_{bond}), lone pair (E_{lp}), valence angle (E_{val}), conjugation (E_{conj}), torsion angle (E_{tors}), and other bond-dependent energies required to properly describe the nature of the stable configurations of molecular systems.

(4) These instantaneous bond orders are subsequently corrected with overcoordination and undercoordination terms designed to favor formation of the proper number of bonds (e.g., 4 for C and Si).

(5) A two-body van der Waals (E_{vdW}) term is included to ensure a proper description of the short-range repulsion due to the Pauli principle and the long-range van der Waals attraction (London dispersion). This applies to all pairs of atoms, including bonded ones. For bonds, this provides the steep two-body repulsion to counter the bond term, which is monotonically attractive.

(6) The ReaxFF partitions the overall system energy into the sum of contributions from various partial energy terms:

$$E_{system} = E_{bond} + E_{lp} + E_{over} + E_{under} + E_{val} + E_{pen} + E_{tors} + E_{conj} + E_{H\text{-}bond} + E_{vdW} + E_{Coulomb}$$

(7) The parameters in this energy expression are fitted to the data from an immense number of QM calculations describing equations of state and reactions of covalent, ionic, and metallic systems. Because ReaxFF is based on QM, we can always test the accuracy of ReaxFF for some new system by comparing back to QM.

The ReaxFF force field has been applied successfully to a vast variety of chemically different systems.[1−8] The ReaxFF parameters employed in this work were reparameterized to fit additional QM data (bond dissociation, geometry distortion, charges, IR-spectra, condensed-phase structure, and equation of state) of H/C/N/O-containing molecules and crystals, including a wide range of reactions for nitramine-[2,3] and peroxide-based[4] energetic materials. For a more elaborate description of the ReaxFF partial energy contributions, see refs 1, 6−8. Here, we employ the ReaxFF parametrization for nitramines used in previous studies of the shock[2] and thermal[3] decomposition of RDX with additional fitting of the parameters to a few initial decomposition reactions in TATB. The actual parameters are included in the Supporting Information.

2.2. ReaxFF-MD Simulations of Thermal Decomposition. The systems studied herein are organic molecular single crystals of HMX and TATB. Of the four temperature-dependent condensed phases of HMX (α, β, γ, and δ), we consider only the β-HMX polymorph (chair conformation), which is the most stable phase under normal conditions. The initial structures of β-HMX and TATB were taken from the Cambridge Structural Database available at the Cambridge Crystallographic Data Centre (http://www.ccdc.cam.ac.uk). Each unit cell was then duplicated in all three directions, by ($4 \times 2 \times 2$) for β-HMX and by ($2 \times 2 \times 4$) for TATB, to provide a supercell with 32 molecules for each system, as shown in Figure 1.

From this structure, we first optimized the atomic positions and cell parameters to minimize the total energy. Then we carried out isothermal−isobaric (NPT) MD simulation (0.2 fs time step) to relax the internal stresses and to obtain the initial

structure (volume V_0) for zero pressure and $T_0 = 300$ K temperature. Here, we used the Berendsen thermostat (50 fs damping constant) and the Berendsen barostat (5000 fs pressure damping constant). After 4 ps of NPT-MD simulation, the equilibrium density was $d_0 = 1.77$ g/cm^3 for β-HMX and $d_0 = 1.88$ g/cm^3 for TATB, in reasonable agreement with the experimental values (1.89 g/cm^3 and 1.94 g/cm^3, respectively).

To investigate the effect of the density increase on chemistry and clustering of carbon in these materials, we created two additional systems for each case with increased densities of $1.3d_0$ and $1.5d_0$ by volumetric compression of the corresponding supercells. These densities are similar to those experienced between the CJ state and von Neumann spike in the detonation wave. Finally, the β-HMX and TATB crystals with three different densities, d_0, $1.3d_0$, and $1.5d_0$, were equilibrated at the initial temperature, $T_0 = 1200$ K, for 4.0 ps using isothermal-isochoric (NVT) MD simulations (time step 0.2 fs). To control the system temperature at the target value, we employed a Berendsen thermostat with a damping constant of 50 fs (characteristic time of the coupling between the thermostat and the system).

After equilibration, we performed a 30-ps NVT-MD (with the same damping constant) on each system at four different temperatures: 1200, 1800, 2400, and 3000 K. The integration time step in the NVT simulations of thermal decomposition was set to 0.1 fs to describe correctly the high-temperature, thermally induced decomposition under homogeneous conditions. This differs from the detonation regime in which the induction time and energy release processes strongly depend on the mechanism of shock compression and heating of the material. In our simulations, the material is quickly heated to very high temperature while avoiding the preceding stage of the shock compression and heating in the detonation wave. Here, we deal with a tiny amount of the material (32 to 128 molecules) kept at the constant temperature and volume, whereas shock experiments are done on substantially larger samples involving a nonhomogeneous reacting medium in which significant mass and heat flows may occur. This results in significant expansion and mixing of the reaction zone. These differences should be taken into account when comparing our computations with experimental measurements on detonating materials.

The algorithm of molecule recognition in the species analysis uses the connection table and bond orders calculated by the ReaxFF at each step and records the molecular components and their compositions every 0.1 ps. In this analysis, the bond order cutoff used to identify molecular species in the systems was set to 0.3 for all atom pairs. Thus, any two fragments were considered separate molecules if all ReaxFF bonds between them have bond orders smaller than 0.3. These data were then used to plot time evolution profiles for reactants, intermediates, and products, providing detailed information about the initiation of chemical reactions and the carbon clustering during the decomposition process. The molecule recognition algorithm also gives information about the structure and elemental composition of carbon clusters formed in the HMX and TATB systems at different densities and temperatures.

3. Results and Discussions

3.1. β-HMX with Various Densities. ***3.1.1. Potential Energy and Total Fragments.*** We performed NVT MD simulations on β-HMX with three different densities—d_0, $1.3d_0$, and $1.5d_0$ (where $d_{0,\beta\text{-HMX}} = 1.77$ g/cm^3 is the equilibrated zero-pressure density)—and four constant temperatures: $T = 1200$, 1800, 2400, and 3000 K. Figure 2 shows time evolution of the potential energy and total number of fragments per single HMX molecule produced in each system.

At 1200 K, we observed no reactions on the time scale of our simulations; hence, we omitted these data from the figures. The plots in Figure 2 reveal the dependence of rate and degree of thermal decomposition on the system temperature and density. In particular, as the system temperature increases, the total potential energy also increases initially in the endothermic process of molecule breakdown until the secondary reactions initiate in partially decomposed solid HMX, which begins to release energy due to the exothermic formation of small molecules. Transition to the energy-releasing state follows after reaching the maximum of the potential energy during the induction (endothermic) stage of the decomposition, and it happens earlier at more elevated temperatures. We estimate the induction time, t_{ind}, for initiation of energy releasing chemical reactions in HMX to be about 4.7, 1.2, and 0.6 ps at density d_0 and 8.6, 2.0, and 0.8 ps at density $1.3d_0 = 2.3$ g/cm^3 for $T =$ 1800, 2400, and 3000 K, respectively.

The rate of potential energy decrease, which is directly related to the exothermic reactions progress, also strongly depends on the temperature and can be fitted to an exponential function,

$$U(t) = U_0 + \Delta q \exp[-(t - t_{ind})/\tau]$$

where U_0 is the asymptotic energy of the products, Δq is the heat of reaction (kcal/mol), and τ is an average characteristic time (i.e., inverse reaction rate) of the energy-releasing reactions. Our simulations provide the following estimates of the characteristic time constants:

- $\tau_{1800} = 109.2$, $\tau_{2400} = 23.0$, and $\tau_{3000} = 8.6$ ps at density d_0;
- $\tau_{1800} = 114.5$, $\tau_{2400} = 30.9$, and $\tau_{3000} = 13.2$ ps at density $1.3d_0$.

However, the number of fragments per molecule at the end of the simulation becomes smaller with the increase in the system density.

For the system with the lowest density, d_0, more fragments are produced at each temperature as compared to simulations with the higher density. This difference might arise because there is less free volume available for generated fragments to move around at higher densities, resulting in a longer induction time and a lower dissociation rate for the HMX molecules. The potential energy may also give a hint: higher temperatures are required at the elevated densities for initiation of the decomposition of HMX molecules. In addition, the molecule fragments and carbon atoms tend to form clusters at higher densities.

3.1.2. Degree of Decomposition. To evaluate the degree of the decomposition of HMX molecules in each system, we count the number of remaining HMX molecules as well as the dissociated NO_2 molecules, as shown in Figure 3. These simulations show that rupture of the N−NO_2 bond accompanied by HONO elimination dominates the initial steps of HMX dissociation. The rate of HMX decomposition increases quickly with temperature, but it slows down at higher densities (particularly, for low temperatures of 1800 and 1200 K), which can be explained by an increase in a N−N bond dissociation energy in the compressed HMX crystal. However, at higher temperatures of 2400 and 3000 K, all HMX molecules in the system decompose very quickly at all densities. For example, it takes about 11, 2.0, and 0.7 ps for undissociated HMX molecules at density d_0 to disappear completely at temperatures 1800, 2400, and 3000 K, respectively. Previous QM studies on HMX reaction pathways[33−35] have also suggested that the first dissociated fragment from a HMX molecule is NO_2.

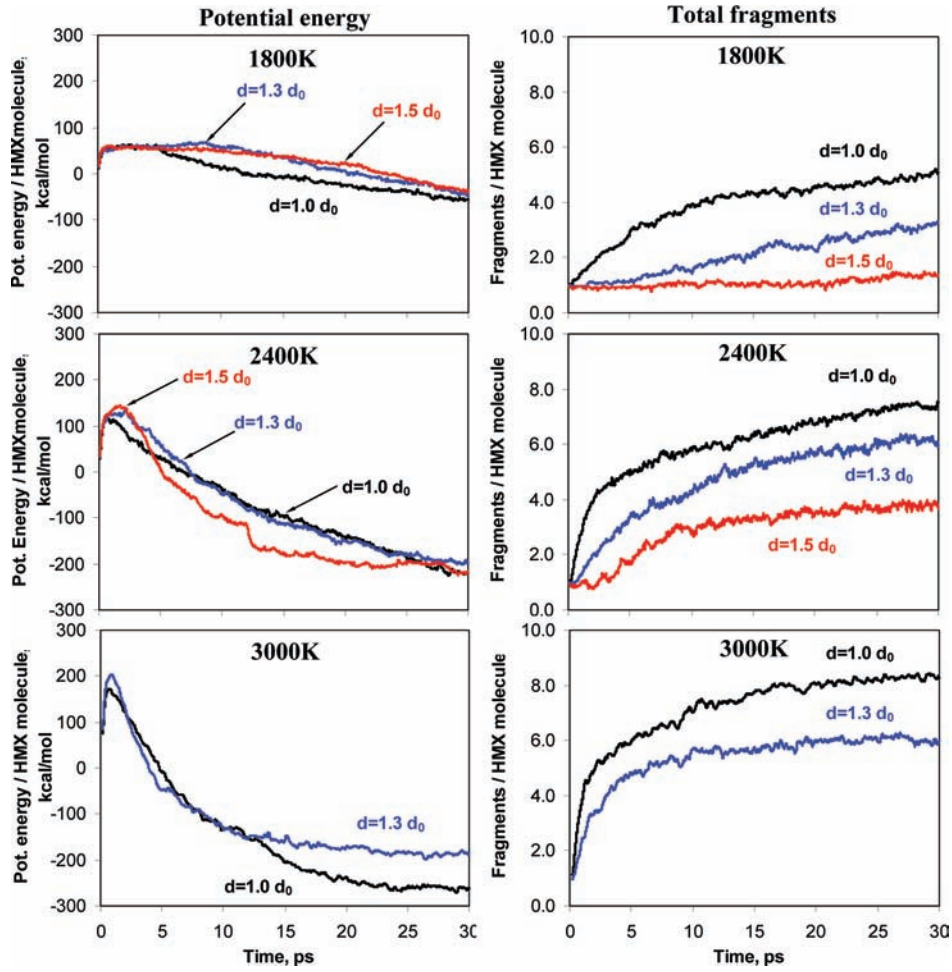

Figure 2. Evolution of potential energy (left column) and total number of fragments per molecule (right column) in MD-NVT simulations of HMX with densities d_0, $1.3d_0$, and $1.5d_0$ (where $d_0 = 1.77$ g/cm^3) and temperatures from 1800 to 3000 K (at $T = 1200$ K, the decomposition was negligibly small).

Evolution of the dissociated NO_2 molecules plotted in Figure 3 (right column) shows clearly that the trends for NO_2 agree with those for the parent HMX molecule: with the increase in the temperature, the rate of NO_2 formation rises quickly, whereas an increase in the density leads to a smaller production of NO_2 fragments. This inhibiting effect of higher density might be explained both by the decrease in the free volume and by the increase in intra- and intermolecular coupling, which causes faster equilibration ("vibrational cooling") of high-frequency modes responsible for the initial endothermic bond breaking reactions.

In addition, the number of NO_2 molecules decreases much more quickly at later times (>5−10 ps) at higher temperature; for example, at 3000 vs 2400 K. This is because more secondary reactions occur at 3000 K than at 2400 K, resulting in a quick consumption of NO_2 molecules and a faster production of stable reaction products, such as N_2, H_2O, CO, and CO_2.

3.1.3. Kinetic Rates. The ReaxFF MD yields kinetic rates of HMX dissociation and energy-releasing reactions in the subnanosecond regime (∼10−100 ps) for temperatures of 1800−3000 K. Due to the absence of chemical kinetic experimental data at such high temperatures, it is difficult to make a direct comparison with ReaxFF calculations. Available experimental data in condensed-phase HE at typical detonation temperatures (∼2000−4000 K) are limited to the nanosecond time resolution measurements of the reaction zone width in detonation waves[47,48] or ignition times of "thermal explosion" (abrupt increase in the temperature) from various thermal-heating experiments.[49−51] These measurements are made over the whole volume and provide only indirect and very approximate estimates of the homogeneous bulk reaction rates due to the heterogeneity of the material (which leads to hot spots and complex multidimensional flows) and large uncertainties in the bulk temperature variations. The experimental data have been used to calibrate the averaged kinetic parameters of chemical decomposition and thermal diffusion in empirical reactive heat transfer and reactive flow ("ignition and growth") models of the initiation and detonation of solid explosives.[52]

Figure 4 displays ReaxFF characteristic times (inverse reaction rates) at normal density (d_0) calculated from the decrease in undissociated HMX molecules at the first endothermic step (inverted triangles) and the potential energy decrease at the second exothermic step (crosses) as a function of inverse temperature. We fit these data using the classical Arrhenius form for the temperature dependence of a first-order reaction rate constant $k = 1/\tau = A \exp[-E_a/RT]$, where τ is a characteristic time, E_a is an activation energy, and A is a frequency prefactor. The solid red lines in Figure 4 are the linear fits to the logarithm of a characteristic time, $\ln(\tau) = (E_a/RT) - \ln(A)$. All parameters are listed in Table 1. Figure 4 also shows the reaction rates for the three-step chemical decomposition model developed by McGuire and Tarver (MT) for HMX[53,54] on the basis of ignition time measurements from weakly and

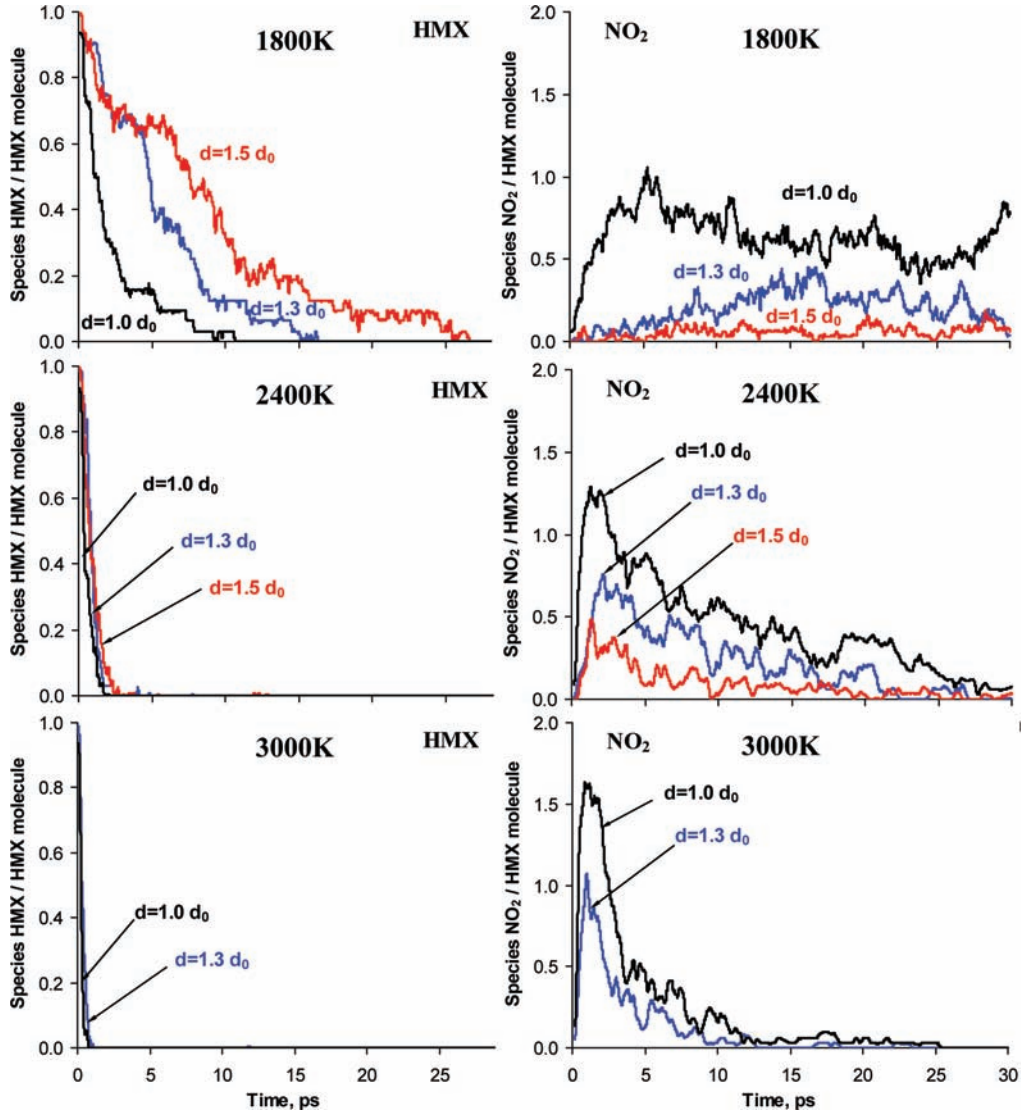

Figure 3. The number of remaining HMX (left column) and dissociated NO_2 (right column) molecules during MD-NVT simulations of HMX decomposition.

heavily confined thermal explosion experiments. These three global reaction steps correspond to

(1) unimolecular endothermic decomposition of the HMX molecule by breaking N−N and C−N bonds;

(2) weakly exothermic unimolecular decomposition of primary fragments into such intermediates as H_2CO, N_2O, HNO_2, HCN; and

(3) highly exothermic gas-phase reactions to produce final, stable products (H_2O, N_2, CO_2, CO, etc.).

The MT model parameters listed in Table 1 have been fitted to reproduce one-dimensional time to explosion (ODTX) in confined experiments. These were recently corrected by Tarver and Tran (TT)[55] to include the β-to-γ solid-phase transition in HMX as a first step and to adjust heats of reactions at subsequent steps. In addition, we include the plots of linear "global rate" dependence derived by Henson from a compilation of ignition times measured in a wide variety of experiments[51] and the decomposition rate estimated by Rogers from his calorimetry experiments near the melting temperature of HMX.[56]

The rate of overall endothermic processes in the first step of ReaxFF simulation (decrease in undecomposed HMX molecules) at 1800−3000 K is reasonably slower than those in Rogers and MT models, which give dissociation times that are too fast (fs and sub-fs) for the temperatures near the von Neumann spike. On the other side, the rate of energy-releasing processes at the second ReaxFF step is about an order faster than estimated either from Henson's single "global rate" model or from the third reaction step of the MT model. Note that a decrease in the material density may reduce considerably the exothermic reaction rate, as shown in previous ReaxFF studies of thermal decomposition of RDX: at a density of $(1/8)d_0$, which shows that the rate decreases by an order of magnitude.[3] The overall energy release, $\Delta q = -1550 \pm 100$ cal/g at the second ReaxFF step, calculated by fitting function the $U(t)$ to the time evolution curve of the potential energy in MD simulations, agrees well with the total heat of the two reaction steps in both MT and TT models.

However, one must be careful in such direct comparisons between the ReaxFF rates and those employed in the empirical models based on the "ignition times". Most of the experimental data were obtained at temperatures below ~600 K, requiring extrapolation of the measured rates to much higher temperatures. Here, additional reaction channels and autocatalytic processes in the solid phase that would invalidate such extrapolations may be activated.

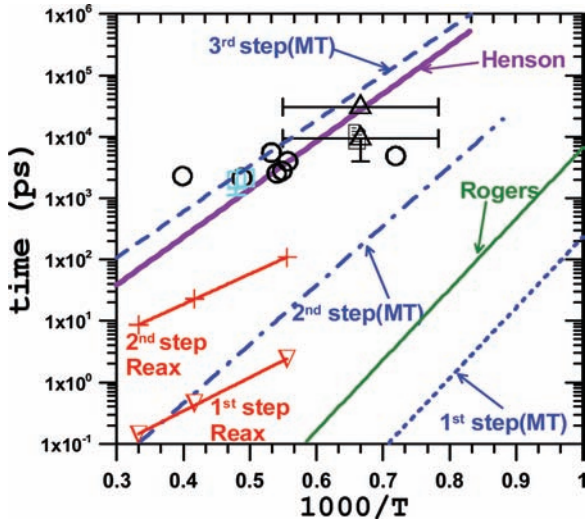

Figure 4. Inverse reaction rates ($\tau = 1/k$) for HMX vs inverse temperature ($1/T$). Thin solid curve (green) uses Rogers' parameters[56] ($E_a = 52.7$ kcal/m, $A = 5.0 \times 10^{19}$ s^{-1}), and thick, solid curve (violet) is Henson's fit[49] ($E_a = 35.6$ kcal/m, $A = 5.6 \times 10^{12}$ s^{-1}). Data from detonation experiments (circles, triangles, and squares) are taken from ref 49.

TABLE 1: Chemical Kinetic Parameters for HMX Decomposition

model	reaction step	frequency factor, ln A (s^{-1})	activation energy, E_a (kcal/m)	heat of reaction, Δq (cal/g)[a]	ref
McGuire-Tarver (MT)	1	48.7	52.7	+100[b]	54
	2	37.3	44.1	−300[b]	
	3	28.1	34.1	−1200[b]	
Tarver-Tran (TT)	1	48.13	48.47	+10[b]	55
	2	48.7	52.7	+60[b]	
	3	37.8	44.3	−133[b]	
	4	28.1	34.1	−1337[b]	
Rogers		45.36	52.7		56
Henson		29.35	35.6		49
ReaxFF	1	33.8	25.1		
	2	29.3	22.6	−1550[c]	

[a] For HMX, cal/g = (kcal/mol)/0.296. [b] At 298 K. [c] At 3000 K, calculated as a decrease in ReaxFF potential energy from its maximum to the asymptotic energy of the products, U_0.

Henson did include additional data from experiments on friction, fast compression and flow, shear ignition, and shock to detonation transition, but the uncertainty of the bulk temperature estimate is quite large, as shown in Figure 4 (open and filled triangles) for ignition times calculated by fitting to the reaction zone width measured in a steady detonation experiment in HMX-based, plastic-bonded explosive PBX 9501. Another set of ignition times (open circles) is based on an indirect estimate deduced from the results of radiometric measurements of the surface temperature evolution in weakly shocked PBX 9404 and assumes that these measurements reflect the true bulk heating processes.

In addition, the parameters for the rate-limiting exothermic reaction step in both multistep models and in the Henson single-step model, which are fitted to the measured ignition times, reflect only an integral behavior of many elemental chemical and physical coupled steps in the decomposition processes. For thermal decomposition of solid explosives with impurities, defects, and polymer binder, the overall "ignition rate" will be controlled by nucleation and growth of the reaction sites and by heat transfer through the heterogeneous interfaces and between the reacted and nonreacted material. Unfortunately, the thermal conductivities at high temperatures in the reacting zone are unknown, so they are usually adjusted ad hoc to get better agreement of the model with overall "ignition times". For shock decomposition, the rates will be also affected by the material deformation and plastic flow under shock compression. All these additional factors, which may result in an extension of the reaction zone, are not present in our ReaxFF 30-ps NVT simulations.

3.1.4. Species Analysis. Figure 5 exhibits the detailed species analysis with the densities d_0 (left column) and $1.3d_0$ (right column) at temperatures 1800, 2400, and 3000 K. For clarity, only components with relatively high abundance are shown in this figure.

We detect the formation of several key products and intermediates of HMX decomposition, such as NO_2, HONO, NO, OH, CH_2O, H_2O, N_2, CO, and CO_2, all of which are also observed in experiment.[36] Of course, our simulation conditions of rather high temperature, absence of a free surface, and fixed volume are quite different from those employed in pyrolysis experiments.

Figure 5 also shows the trend in how these components change with the system temperature and density. In particular, both primary decomposition products NO_2 and HONO are produced faster and in larger quantities at higher temperatures, but NO_2 formation is the dominant reaction at early times, especially for low temperature ($T = 1800$ K). This difference is expected because of its lower activation barrier and larger pre-exponential factor (i.e., larger activation entropy) for the NO_2 rate constant as compared to the HONO elimination.[33,34]

We also observed other intermediates and products, such as HNO, HCN, HNCO, HNO_3, NO_3, and N_2O, but their concentrations remain lower than 0.1−0.2 (per single HMX molecule) since they are rapidly consumed by the secondary reactions. We find that the formation of NO, H_2O, and N_2 begins shortly after the initial dissociation of NO_2 and at about the same time as HONO. The population of final products at 30 ps (H_2O, N_2, CO, and CO_2) increases dramatically with temperature, thereby increasing the energy release.

The rate of H_2O formation is faster than that of N_2, although the difference becomes much less pronounced at the highest temperature, $T = 3000$ K, and for higher density. Quantum MD using the density functional tight-binding (DFTB) method used to simulate constant-temperature decomposition of the δ-phase of HMX (with boat molecule conformation) at similar conditions (3500 K, 2.1 g/cm^3) has also exhibited faster formation of H_2O vs N_2, but with a larger rate difference.[37]

We fitted the time evolution of the abundances of final products to an exponential function,

$$C(t) = C_\infty(1 - \exp[-kt])$$

where C_∞ is the asymptotic abundance value, and k is the effective rate constant of the product formation. Table 2 shows that the reaction rates for the formation of H_2O, N_2, CO_2, and CO in HMX obtained from ReaxFF NVT simulations at normal and increased densities are in reasonable agreement with the results of DFTB MD simulation.

We find that at low temperatures, the initiation of the formation of N_2 and H_2O is delayed at higher density (e.g., at 1800 K and $1.3d_0$), although their populations grow up to comparable values at the end of the simulation (30 ps) for both normal and 30%-increased densities, as shown in Figure 3. The populations of CO and CO_2 molecules exhibit opposite trends in their density dependence: the formation of CO is suppressed

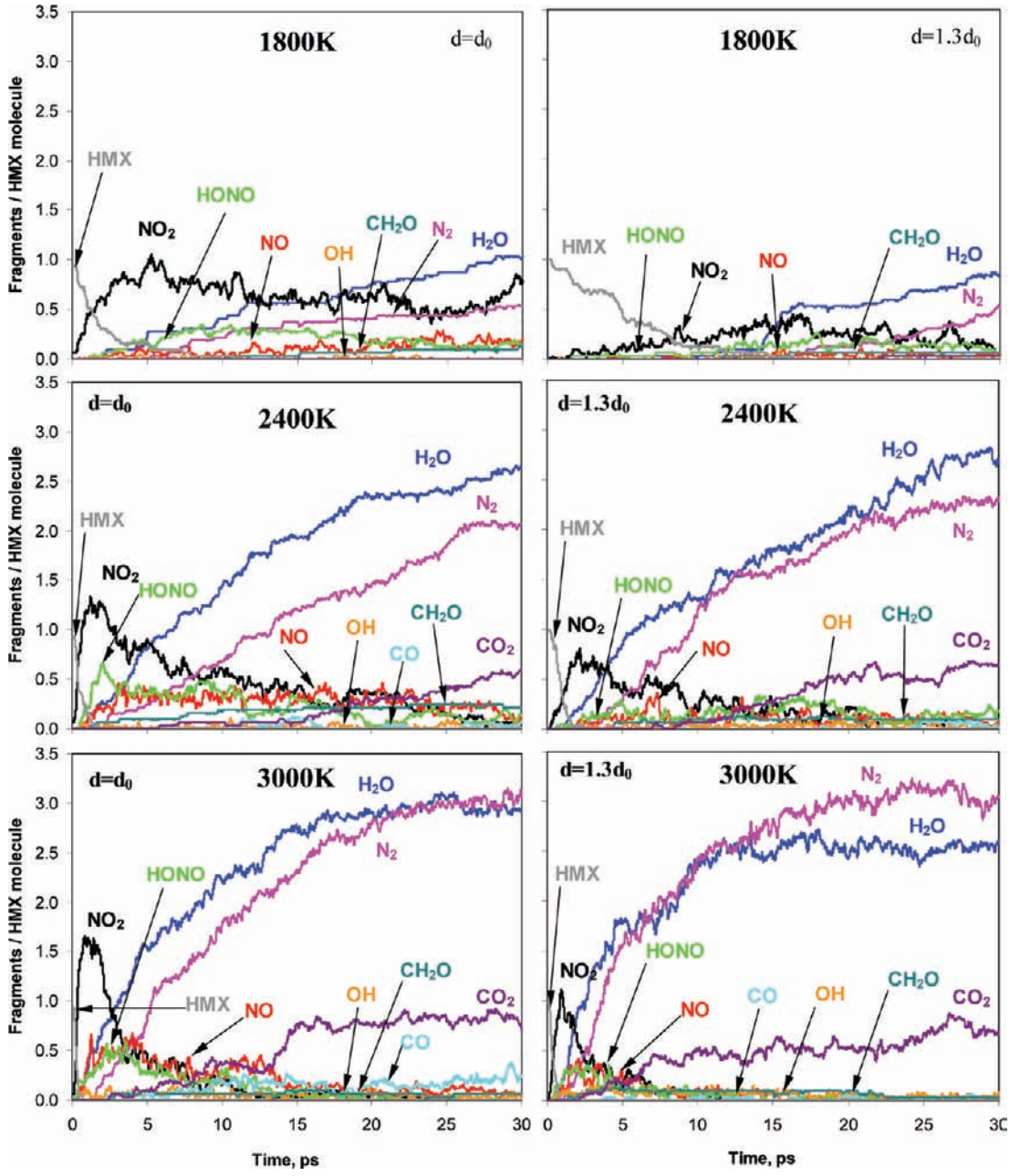

Figure 5. Evolution of intermediate and secondary products of HMX decomposition for two densities: $d_0 = 1.77$ g/cm^3 (left column) and $1.3d_0 = 2.30$ g/cm^3 (right column).

TABLE 2: Reaction Rate k (ps^{-1}) of Final Products Formation in HMX[a]

model	H_2O	N_2	CO_2	CO
DFTB, 3500 K, 2.1 g/cm^3	0.48	0.08	0.05	0.11
ReaxFF, 3000 K, 1.77 g/cm^3	0.14	0.08	0.05	0.06
ReaxFF, 3000 K, 2.3 g/cm^3	0.23	0.15	0.11	

[a] Density functional tight binding (DFTB) MD results are for δ-HMX.[37]

at elevated density for all temperatures, whereas the CO_2 formation proceeds relatively faster, particularly at the expense of CO molecules. However, the total number of CO_2 molecules reaches about the same value at 30 ps for both densities, which can be explained by a competition between faster formation of CO_2 and a tendency of carbon atoms to form condensed-phase aggregates at higher density.

The formation of final products is not fully completed within 30 ps of the simulation time, especially for the low-temperature cases, and their abundances keep changing if the simulation continues. Table 3 compares the product distribution at the end of the 30-ps simulation at 3000 K and d_0 (where the secondary reactions are most completed) with the results obtained from the 55-ps quantum/DFTB MD simulation[37] and from the calorimeter bomb experiment.[57,58]

The ReaxFF results also include the asymptotic product abundances, C_∞, obtained by the aforementioned exponential fit. Although the total number of N_2 and H_2O molecules formed agrees well with both experimental and DFTB MD results, the predictions for CO_2 and especially for CO exhibit less agreement. We assume that this is because the CO_2 and CO molecules remain agglomerated into small clusters containing a considerable number of carbon and oxygen atoms, as indicated by the elemental composition of residues in Table 3. In the calorimetric experiment, the products would undergo isentropic expansion, but our constant-volume simulations do not allow this. If

TABLE 3: Final Products of the Decomposition of β-HMX[a]

products (mol/mol)	DFTB; 55 ps, 3500 K, 2.1 g/cm^3	ReaxFF; 30 ps, 3000 K, 1.77 g/cc	ReaxFF; asymptote, C_∞	experiment (confined);[58] 1.89 g/cm^3
N_2	3.03	3.03	3.51	3.68
H_2O	2.87	2.91	3.08	3.18
CO_2	0.97	0.72	1.27	1.92
CO	1.90	0.22	0.39	1.06
C(s)				0.97
NH_3		0.16	0.28	0.395
H_2		0.06		0.30
CHNO	0.34	0.22		
HCN				0.008
CH_4				0.039
C_2H_6				0.001
residues (%)[b]				
C		71.1		
H		18.0		
N		19.5		
O		40.2		

[a] Density-functional tight binding (DFTB) MD results are for δ-HMX.[37] [b] Number of atoms (% of system total) in small agglomerates. For example, $C = 0.711 \times 128 = 91$ carbon atoms.

expansion had been allowed, we expect that these agglomerates would decompose with additional formation of CO_2 and CO. Indeed, our previous ReaxFF NVT simulations of RDX at normal and 8-fold reduced densities[3] indicate that the CO production at the same temperature greatly increases with a decrease in the density.

3.1.5. Carbon-Rich Clusters. Experimental studies have shown that carbon clusters can be formed in detonation of carbon-rich explosives.[19−27] Kinetic mechanisms have been developed to characterize the formation of such clusters at the front of the detonation wave and their influence on the properties of the reaction zone.[28−32] From molecule recognition analysis, we can identify all possible species and clusters (using the bond order cutoff of 0.3 to determine the atom connectivity). To study the cluster formation kinetics, we focused on the evolution of the cluster with the maximum molecular weight (called "maximum cluster") at each time frame for each system.

Figure 6 shows time evolution of the molecular weight of the maximum cluster in β-HMX for the three densities studied here and temperatures of 1200, 1800, 2400, and 3000 K. In the crystals with normal density d_0, only small clusters are observed during all the simulation time, but in the system with elevated densities ($1.3d_0$ and $1.5d_0$), much larger carbon-reach aggregates are formed. With an increase in the simulation temperature, the size of the maximum cluster abruptly jumps to a molecular weight of about 1500 amu at 1800 K ($1.3d_0$) and 4800 amu at 2400 K ($1.5d_0$). However, we found that these clusters are unstable and break apart soon after the initiation of secondary reactions and formation of small carbon-containing radicals and molecules, such as CO_2 and CO.

To analyze the elemental composition of the largest aggregates formed during the simulations, we calculated the elemental ratios H:C, O:C, and N:C, and traced their evolution as shown in Figure 7a (d_0) and 7b ($1.3d_0$) for all temperatures. For convenience, the molecular weights of the maximum clusters (corresponding to the right axis in each figure) are also plotted in these figures.

At the equilibrium density d_0, no clusters were found at 1200 and 1800 K, but the formation of some small aggregates (with a mass less than the mass of two HMX molecules) was observed at 2400 and 3000 K. Although the total mass of these clusters exhibits no significant fluctuations, they contain fewer hydrogen and nitrogen atoms at the end of the simulations. The nitrogen atoms have a tendency to leave the cluster more quickly with

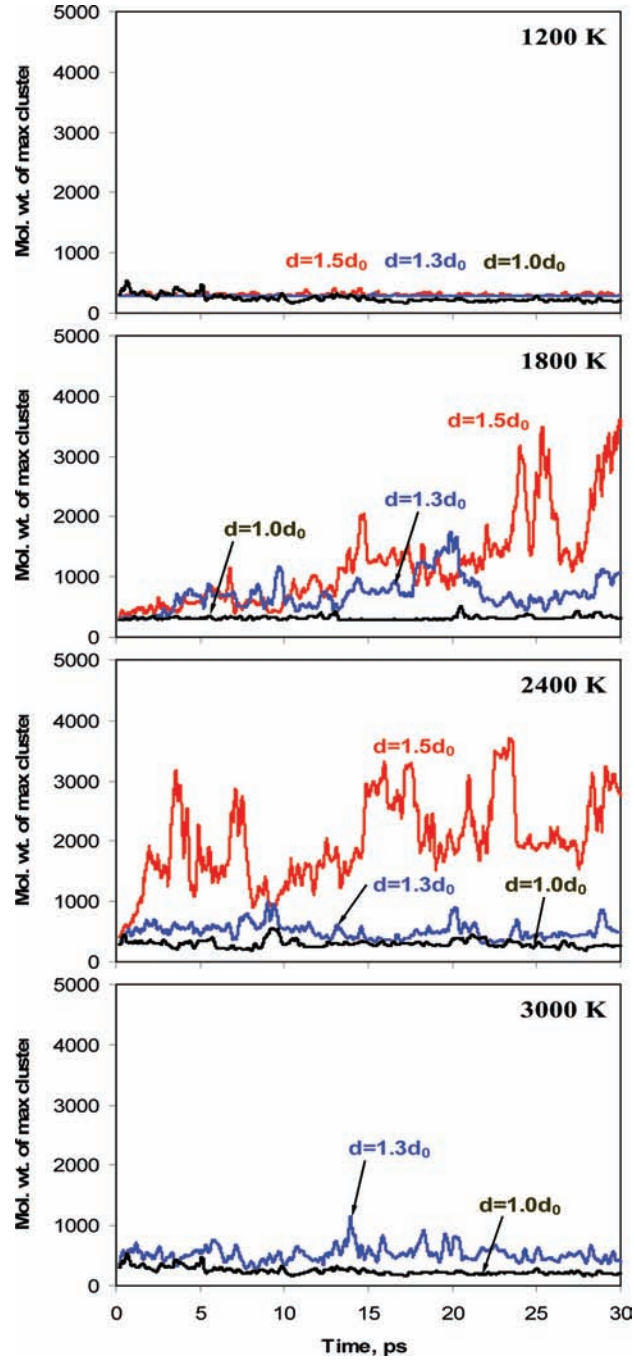

Figure 6. Time evolution of a weight of largest carbon cluster formed during HMX decomposition at different densities (d_0= 1.77 g/cm^3) and temperatures (HMX molecule mass m_{hmx} = 296 amu).

increased temperature and the oxygen demonstrates more complicated behavior. The rate of oxygen dissociation, especially at normal density, is faster than that for nitrogen or hydrogen. However, at the highest temperature (3000 K), oxygen tends to migrate back to the cluster after initial dissociation (particularly because of the coagulation of carbon radicals and small molecules), so the ratio between remaining oxygen and nitrogen atoms gets reversed.

In the system with a higher density ($1.3d_0$), no clusters were formed at 1200 K either, but a few clusters bigger than in the $1.0d_0$ case were found at temperatures 1800, 2400, and 3000 K. These clusters also exhibit a lower content of H, N, and O atoms at higher temperatures, which slowly decreases in time so that more carbon atoms will remain aggregated. However,

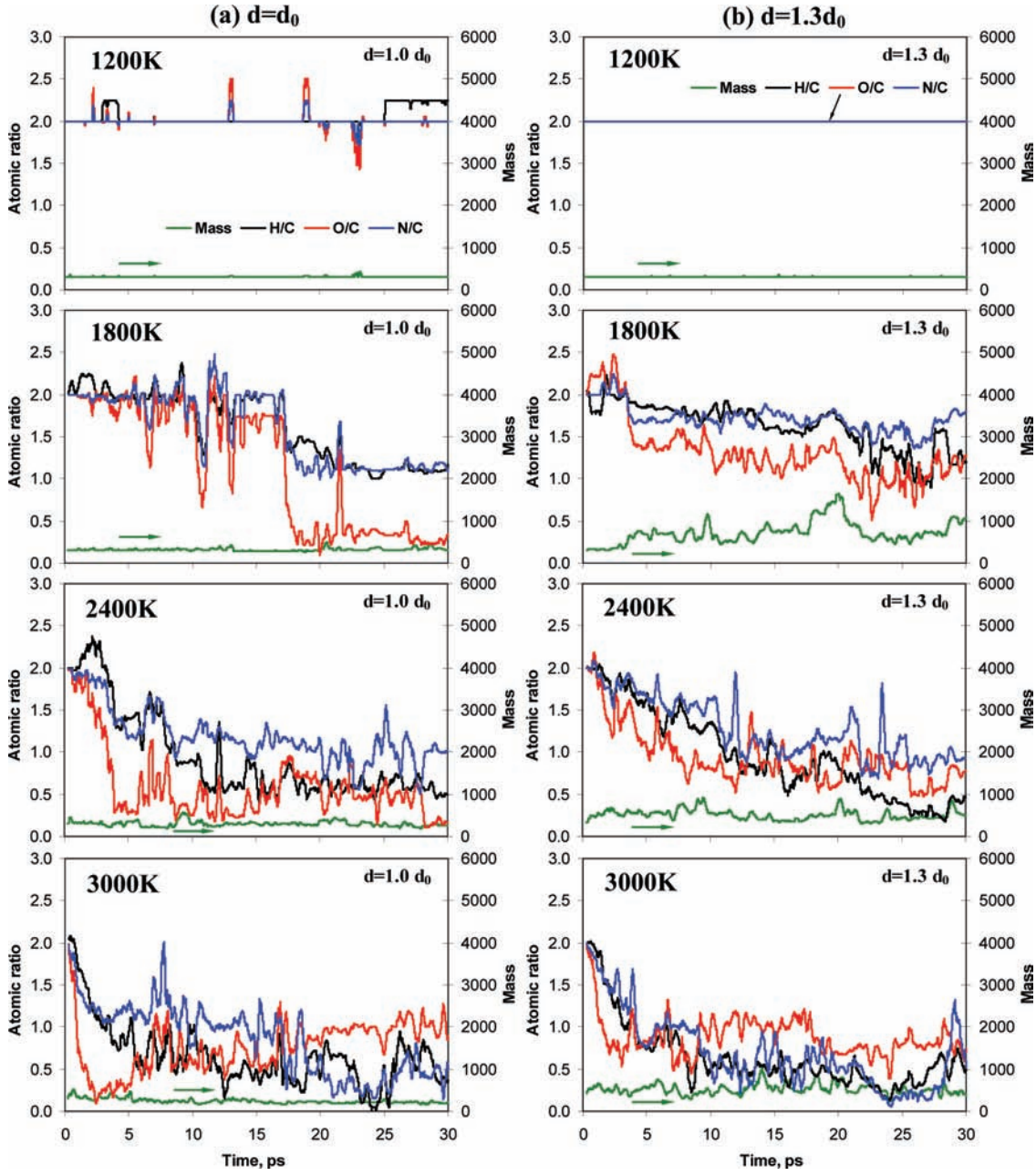

Figure 7. Fluctuations in the elemental composition (H:C, black line; O:C, red line; N:C, blue line) and molecular mass (green line) during formation of largest carbon cluster in HMX for various temperatures and densities: (a) $d_0 = 1.77$ g/cm^3 and (b) $1.3d_0 = 2.30$ g/cm^3.

the stability of large clusters appears to reduce as the temperature goes up: the maximum cluster with the molecular weight of ~1000 amu exists up to the end of the simulation at a moderate temperature (~1800 K), but it breaks apart at higher temperatures.

3.2. TATB with Various Densities. ***3.2.1. Potential Energy and Total Fragments.*** We carried out NVT-MD simulations similarly to those for HMX to study the thermal decomposition of the TATB crystal for the same set of temperatures (1200−3000 K) and densities ($1.0-1.5d_0$) with the equilibrated zero-pressure density of $d_{0,\mathrm{TATB}} = 1.88$ g/cm^3. Figure 8 displays the evolution of the potential energy per TATB molecule (left column) and the total number of decomposition products (right column) produced at various densities and temperatures. The induction time, t_{ind}, for the initiation of energy-releasing chemical reactions in TATB is 3−5 times longer than that for HMX: at density d_0, we obtain $t_{\mathrm{ind}} = 5.6$ for 2400 K and 2.0 ps for 3000 K; and at density $1.3d_0 = 2.45$ g/cm^3, we obtain $t_{\mathrm{ind}} = 9.0$ for 2400 K and 2.8 ps for 3000 K. However, in contrast to the HMX case, we did not detect the energy release in TATB during 30-ps simulation at 1800 K. The maximum of the potential energy attained during the induction period for TATB increases monotonically with the temperature, as in the HMX case, but its density dependence shows quite a different behavior from that for HMX. As the density increases from d_0 to $1.3d_0$, the potential energy maximum attained during the initial steps of the TATB dissociation also increases. However, it decreases much more as the density is increased to $1.5d_0$, in contrast to the HMX case; this happens because at higher density, it is favorable for TATB molecules to dimerize (which is endothermic but has an activation energy lower than that of the homolytic bond cleavage in TATB[38]), which is reflected in the decrease in the total number of fragments in the beginning of the simulation (see Figure 8b).

3.2.2. Degree of Decomposition. The abundance ratios of undecomposed TATB molecules and dissociated NO_2 radicals observed during the simulations are shown in Figure 9 (left

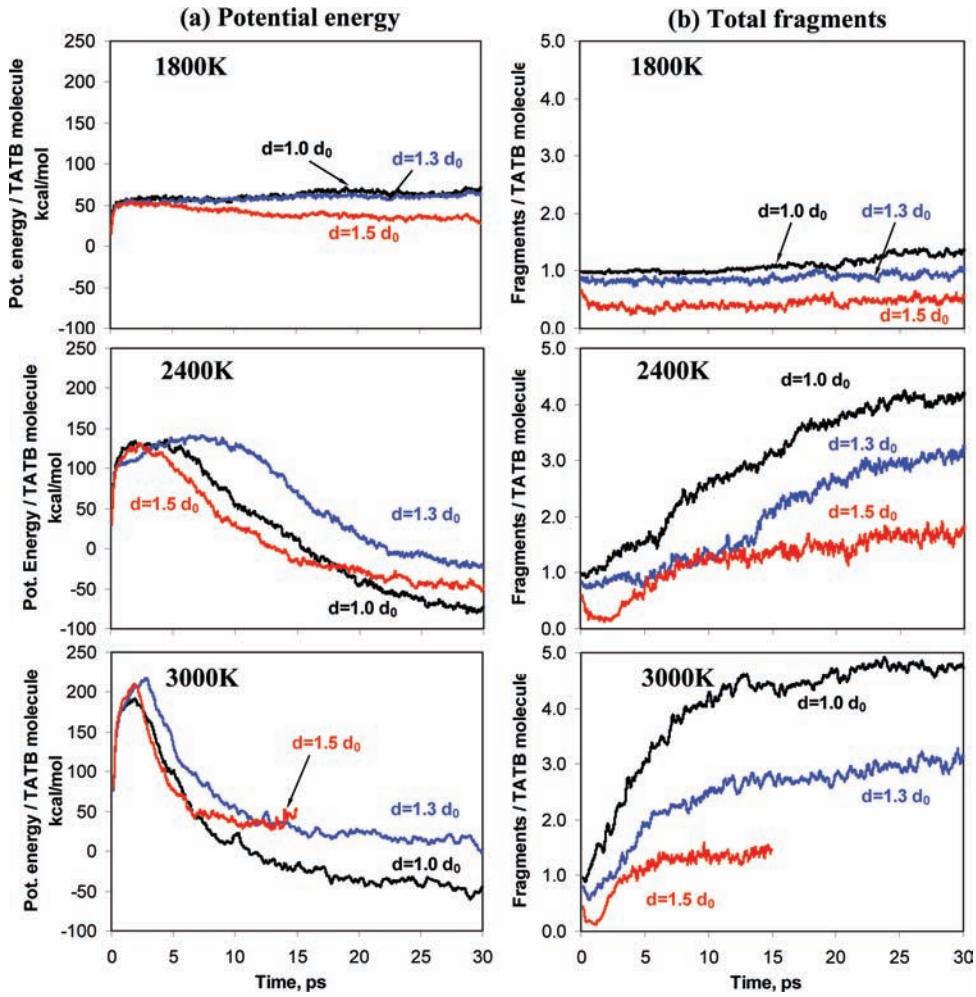

Figure 8. Evolution of potential energy (left column) and total number of fragments per molecule (right column) in MD-NVT simulations of TATB for densities d_0, $1.3d_0$, and $1.5d_0$ (where $d_0 = 1.88$ g/cm^3) and temperatures from 1800 to 3000 K (at $T = 1200$ K, the decomposition was negligibly small).

column, TATB; right column, NO_2). As the temperature increases to 2400 K, the decomposition rate of TATB is greatly increased so that all TATB molecules in the systems decompose very quickly (in about 8.7 and 3.0 ps at 2400 and 3000 K, correspondingly). In contrast, at 1800 K, the decomposition proceeds much more slowly, with ~25% of the TATB molecules remaining intact at the end of 30-ps simulation. Some of this decrease in the loss of TATB molecules is the formation of TATB dimers.

The simulations show also that with the increase in the density from d_0 to $1.3d_0$, the rate of decrease in the number of TATB molecules in the system becomes slower by ~40%, whereas in the case of HMX decomposition, the rate drop is ~140%. However, for TATB, this decomposition becomes much faster at the highest density of $1.5d_0$, as compared with $1.3d_0$, which is different from the monotonic trend observed for HMX in Figure 3. The additional decrease in the number of remaining TATB molecules results from the activation of the dimerization reaction at higher densities and correlates with the above-discussed decrease in the potential energy maximum due to the lower activation barrier.

The dissociation of the intermediate NO_2 exhibits a well-pronounced increase with temperature, especially for density d_0. Similar to the HMX simulations, the number of NO_2 molecules decreases more quickly at higher temperatures because of the acceleration of secondary reactions, as seen in Figure 9. On the other hand, the production of NO_2 becomes negligible at 1800 K, although TATB molecules still continue to decompose, which indicates the existence of alternative mechanisms of TATB decomposition at low temperatures. The increase in the density imposes a relatively stronger inhibiting effect on NO_2 dissociation than in the case of HMX and, in addition, leads to a significant increase in its induction time, which might be explained by activation of the competitive dimerization reaction.

3.2.3. Kinetic Rates. Figure 10 displays an inverse global rate of the first endothermic step (inverted triangles) at density d_0 and temperatures varying from 1900 to 3000 K, calculated from ReaxFF MD as the rate of decrease in undissociated TATB molecules.

Similarly, a global rate of the second exothermic step (crosses) is calculated as the rate of the potential energy decrease fitted to the same exponential function as in the previous HMX case. These rates plotted in logarithmic scale are then fitted to the linear Arrhenius dependences shown by solid red lines with parameters listed in Table 4.

Figure 10 also displays the linear rate dependencies on temperature used in the three-step empirical model of Tarver et al. for TATB decomposition.[54] The first two steps in this model are endothermic, and only the third reaction of the formation of final gaseous products is exothermic. However, in the previous model of McGuire and Tarver, both the second

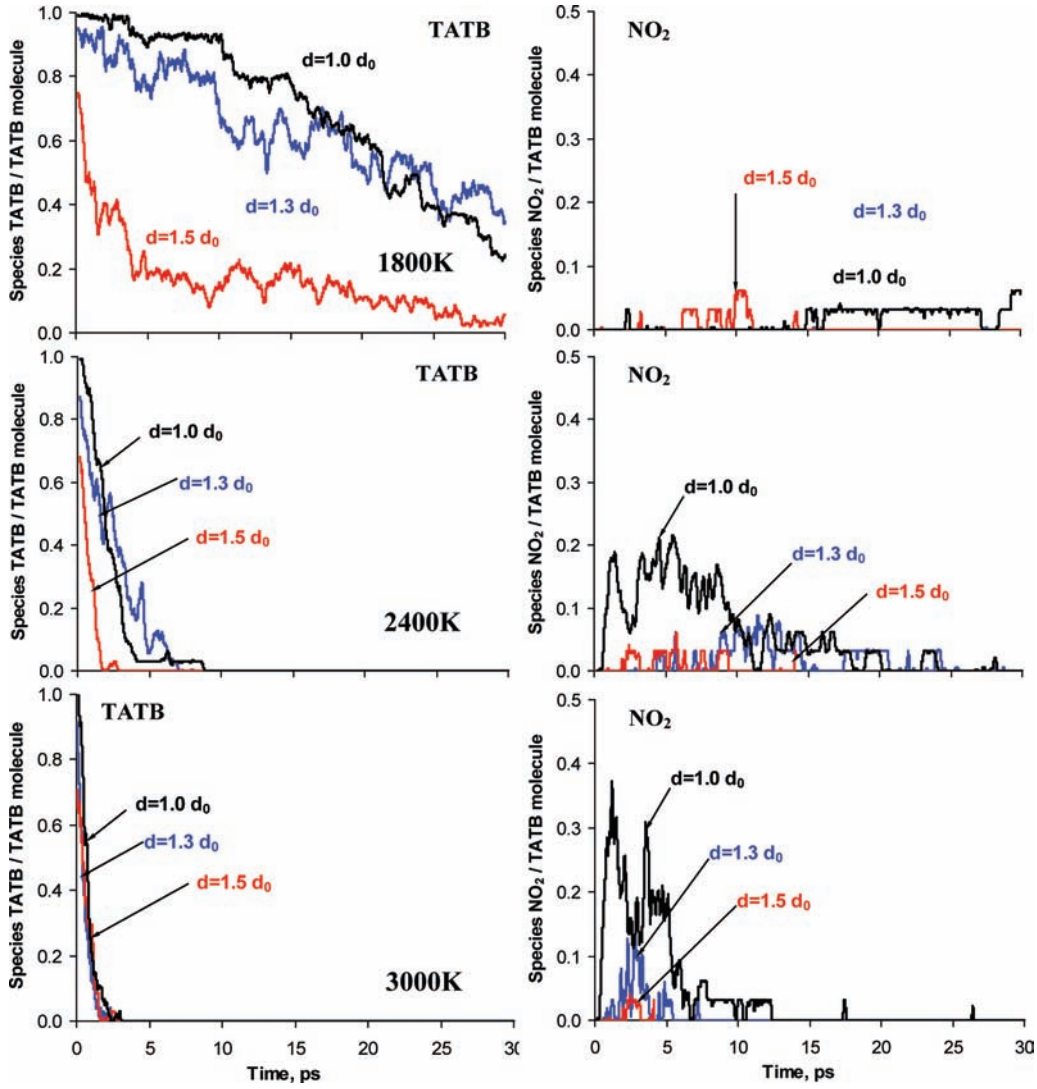

Figure 9. The number of remaining TATB (left column) and dissociated NO_2 (right column) molecules during MD-NVT simulations of TATB decomposition.

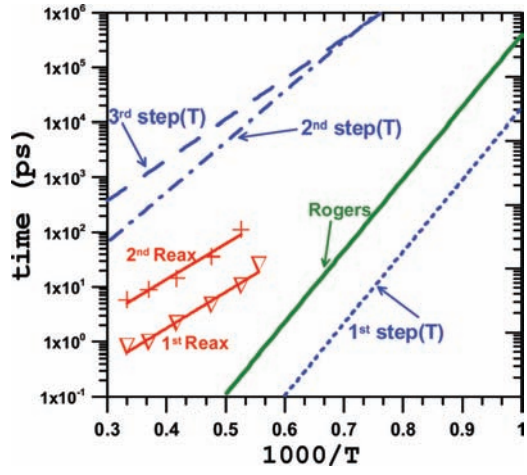

Figure 10. Inverse reaction rates ($\tau = 1/k$) for TATB vs inverse temperature ($1/T$). Solid curve (green) uses Rogers' parameters[56] (E_a = 59.9 kcal/m, $A = 3.18 \times 10^{19}$ s^{-1}) and dotted, dashed-dotted, and dashed curves (blue) correspond to the first, second, and third steps, respectively, in the chemical decomposition model of Tarver et al.[54]

and third steps were exothermic.[53] Figure 10 also shows Rogers's rate of TATB decomposition extrapolated from the low-temperature calorimetry experiments.[56]

TABLE 4: Chemical Kinetic Parameters for TATB Decomposition

model	reaction step	frequency factor, ln A (s^{-1})	activation energy, E_a (kcal/m)	heat of reaction, Δq (cal/g)[a]	ref
McGuire-Tarver (MT)	1	29.5	42.0	+50[b]	53
	2	45.0	60.0	−900[b]	
	3	35.0	54.0	−950[b]	
Tarver et al. (TCN)	1	48.0	60.0	+50[b]	54
	2	29.8	42.0	+50[b]	
	3	26.8	33.8	−700[b]	
Rogers		44.906	59.9		56
ReaxFF	1	33.2	30.2		
	2	31.0	29.7	−910[c]	

[a] For TATB, cal/g = (kcal/mol)/0.258. [b] At 298 K. [c] At 3000 K, calculated as a decrease in ReaxFF potential energy from its maximum to the asymptotic energy of the products, U_0.

The global rate of endothermic reactions at the first ReaxFF step is much slower (by 1−4 orders, depending on temperature) than the fs^{-1} and sub-fs^{-1} rates used in both the Rogers and TCN models. In contrast, the rate of energy release at the second ReaxFF step is about 2 orders faster than at the third step of the TCN model. This might be due to the relatively fast formation of water in ReaxFF simulations, which begins after 10 ps at 1800 K (which is lower than the value observed in

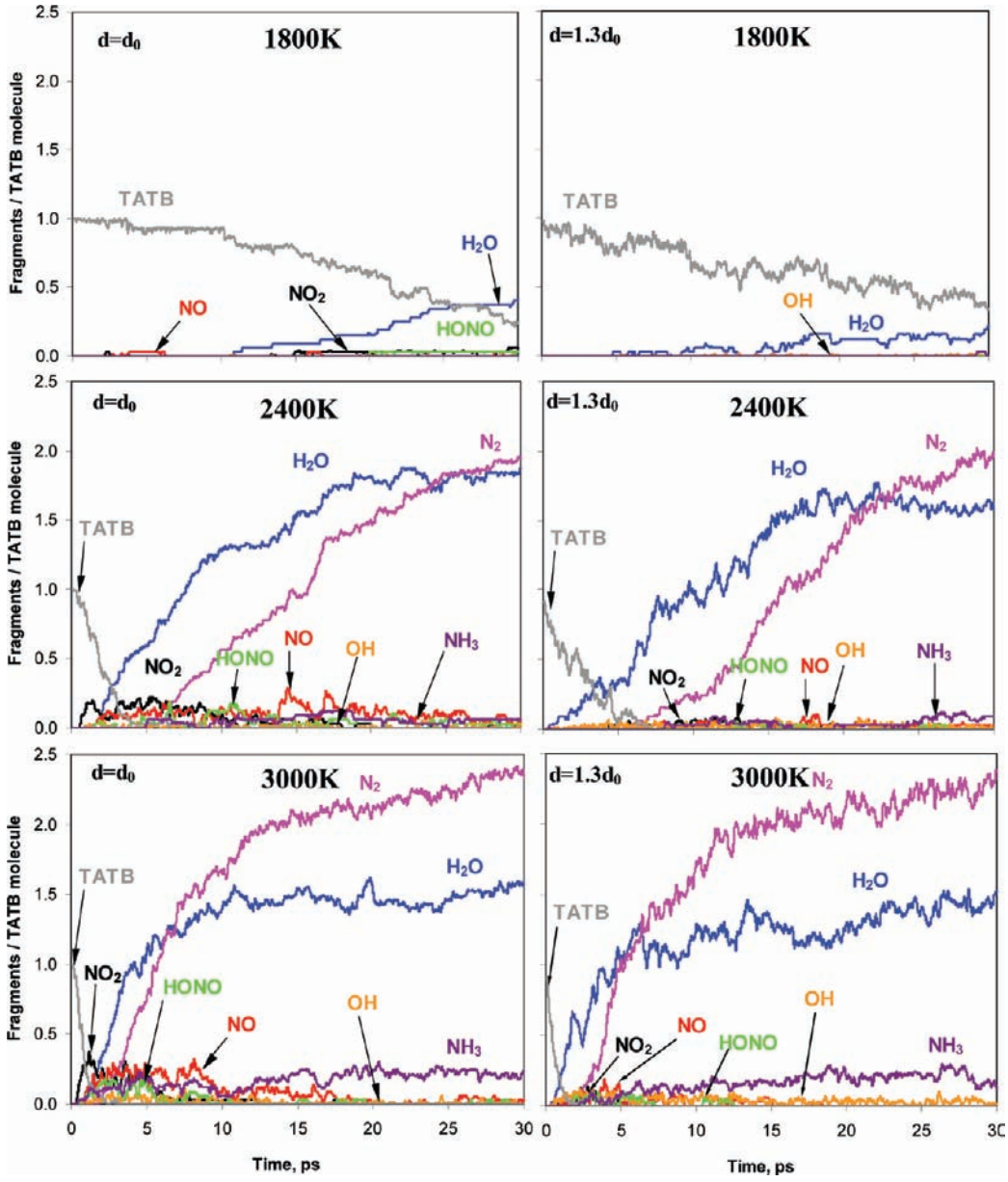

Figure 11. Evolution of intermediate and secondary products of TATB decomposition for two densities: $d_0 = 1.88$ g/cm^3 (left column) and $1.3d_0 = 2.44$ g/cm^3 (right column).

recent DFTB MD simulations[59]). By fitting the time evolution of the potential energy to an exponential function $U(t)$, we estimate the overall energy release at the second ReaxFF step, $\Delta q = -(910 \pm 70)$ cal/g. This agrees with the measured heat of detonation, -1020 cal/g,[51,52] but less well with the third step of the TCN model (-700 cal/g).

3.2.4. Species Analysis. Figure 11 shows a detailed species analysis for TATB with densities d_0 (left column) and $1.3d_0$ (right column) at 1800, 2400, and 3000 K for the products with relatively high concentrations, such as NO_2, NO, HONO, H_2O, N_2, NH_3, and OH that exhibit substantial dependence on the system temperature and density. At the lowest temperature of 1800 K, we observed only a few primary dissociation species—OH, NO, HONO, and NO_2—followed by very slow formation of H_2O molecules. The abundances of nitrogen-containing products NO_2, HONO, and NO are about the same (whereas HMX had much more NO_2), and all are much smaller than those in HMX.

For TATB, the formation of H_2O molecules begins at about the same time as OH and before the appearance of NO_2 and HONO fragments. Thus, the ReaxFF simulations indicate that C$-$NO$_2$ bond cleavage is not the dominant pathway for the first step of TATB dissociation and that the initial steps (especially at low temperatures) may involve other reactions; for example, the hydrogen transfer, as suggested by Wu and Fried.[39] Between 1800 and 2400 K, we find an abrupt increase in the rate of energy release (see Figure 8a) which correlates well with much faster formation of water molecules.

In addition, new secondary products, such as N_2 and NH_3 (not observed during 30-ps simulation at 1800 K) appear at higher temperatures of 2400 and 3000 K, contributing significantly to a large increase in the exothermic heat. We also observe faster formation of intermediates NO_2, HONO, and NO (but not OH) as the temperature increases. The rate of H_2O formation is faster than that of N_2, although the difference becomes quite small at the highest temperature of 3000 K, as in the case of HMX simulations. Similarly, the density increase from d_0 to $1.3d_0$ inhibits the formation of the intermediates and small carbon-containing molecules, although it does not affect much the N_2 and H_2O populations at the end of the simulation.

TABLE 5: Final Products from the Decomposition of TATB

products (mol/mol)	ReaxFF; 30 ps, 3000 K, 1.88 g/cc	ReaxFF; asymptote, C_∞	experiment (confined);[57] 1.87 g/cm^3
N_2	2.34	2.34	2.34
H_2O	1.56	1.50	2.08
CO_2	0.28	0.40	1.95
CO	0.09		0.40
C(s)	4.50[a]		3.61
NH_3	0.25	0.26	0.11
H_2	0.13		0.086
HCN	0.03		0.014
CHNO	0.13		
CH_4			0.026
residues (%)[b]			
C	91.1		
H	28.6		
N	15.1		
O	60.9		

[a] Total number of carbons in two biggest clusters: $C_{107}H_{31}O_{64}N_{12}$ and $C_{37}H_9O_{27}N_3$ [b] Number of atoms (% of system total) in carbonaceous clusters and small agglomerates, including those in C(s) clusters. For example, $C = 0.911 \times 192 = 175$ carbon atoms.

However, in contrast to HMX, we found almost no CO and a very few CO_2 molecules, despite TATB's having 50% more carbon atoms than HMX. This results because TATB decomposition leads to formation of copious amount of large molecular clusters dominated by carbon atoms, leading to carbon-poor gaseous products, as shown by the bond-order analysis of their composition. As the density increases, the equilibrium population of CO and CO_2 molecules decreases practically to zero due to intensification of the processes of solid carbon coagulation.

As shown in the next sections, carbon clusters in TATB capture a significant amount of oxygen and, to a lesser extent, nitrogen atoms, suspending the formation of final gaseous products and complete energy release. The first, "fast" stage of energy release in ReaxFF simulations is related to a quick formation of water followed by slower generation of N_2 molecules. When most of H_2O and N_2 species are formed, the energy release enters the "slow" stage in which the captured atoms are slowly released from the clusters, which continue their further coagulation into carbon soot.

Table 5 shows the final products observed at the end of the simulation at d_0 and 3000 K as compared with the products from the postdetonation calorimeter bomb experiment.[51,52] We stress that the formation of solid carbon residue and gaseous products is not completed on the time scale of our simulations, which focuses on the initial and intermediate stages. In addition, our simulations are performed at constant volume and temperature, whereas the experimental measurements are made in the postdetonation phase after isentropic expansion and cooling of the products.

The asymptotic product abundances, C_∞, are obtained by exponential fit to the product evolution curves. Both observed and asymptotic numbers of N_2 molecules are in good agreement with experiment, but the water formation is underestimated. In addition, there is a significantly smaller number of formed CO_2 and CO molecules which remain agglomerated into much bigger carbonaceous clusters than in HMX. If we continue the simulation with linear-rate expansion of the volume, an increase in the CO_2 and CO abundances is observed.

3.2.5. Carbon-Rich Clusters. At every time step in each simulation, we calculate the molecular weights of the clusters and choose a cluster with the maximum weight (called "maximum cluster"). Figure 12 shows how the molecular weight

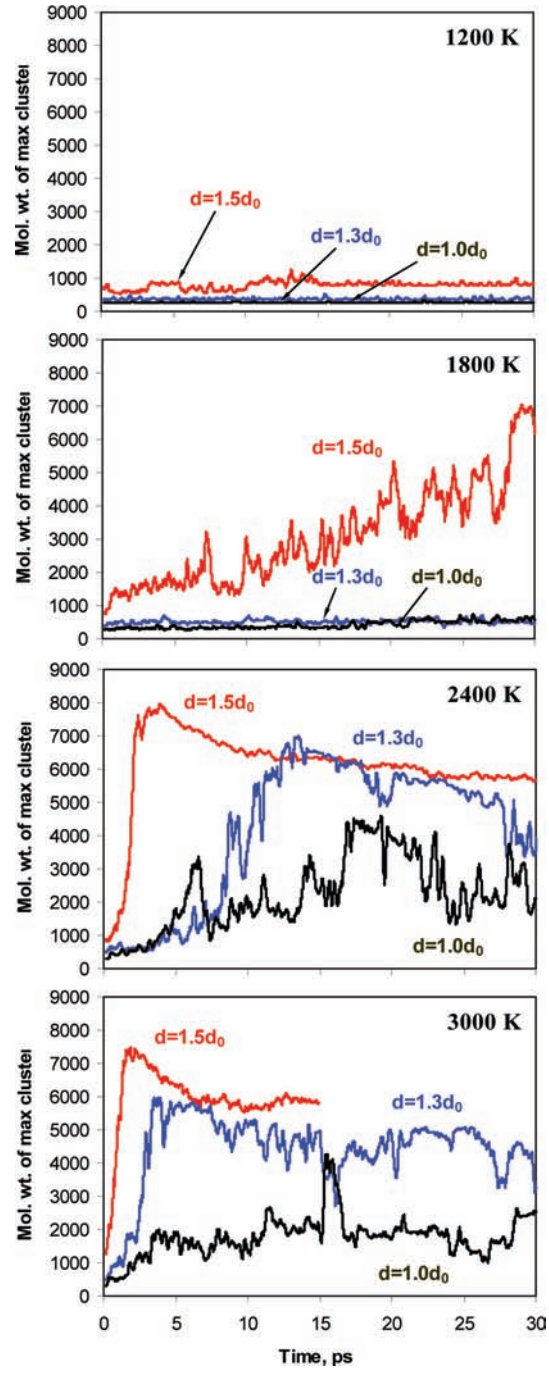

Figure 12. Time evolution of a weight of the largest carbon cluster formed during TATB decomposition at different densities ($d_0 = 1.88$ g/cm^3) and temperatures (TATB molecular mass $m_{tatb} = 258$ amu).

of this maximum cluster changes with time in the TATB system with various densities and temperatures. In the systems with normal d_0 and 30%-elevated densities, no clusters form at 1200 and 1800K (there are no reactions at all for 1200 on the 30-ps time scale). However, at higher temperatures (2400 K and above), we observe the appearance of stable carbon-rich aggregates with large molecular weight up to 2000−4000 amu (equivalent to about 8−15 molecules of TATB).

For the highest density, $1.5d_0$, the formation of clusters begins at the lower temperature 1800 K and proceeds much faster than at lower densities as the temperature increases to 2400 K and beyond. The molecular weight of the maximum cluster in the 50%-compressed system initially reaches 7800 amu at 2400 K and 7400 amu at 3000 K. The maximum clusters in TATB are

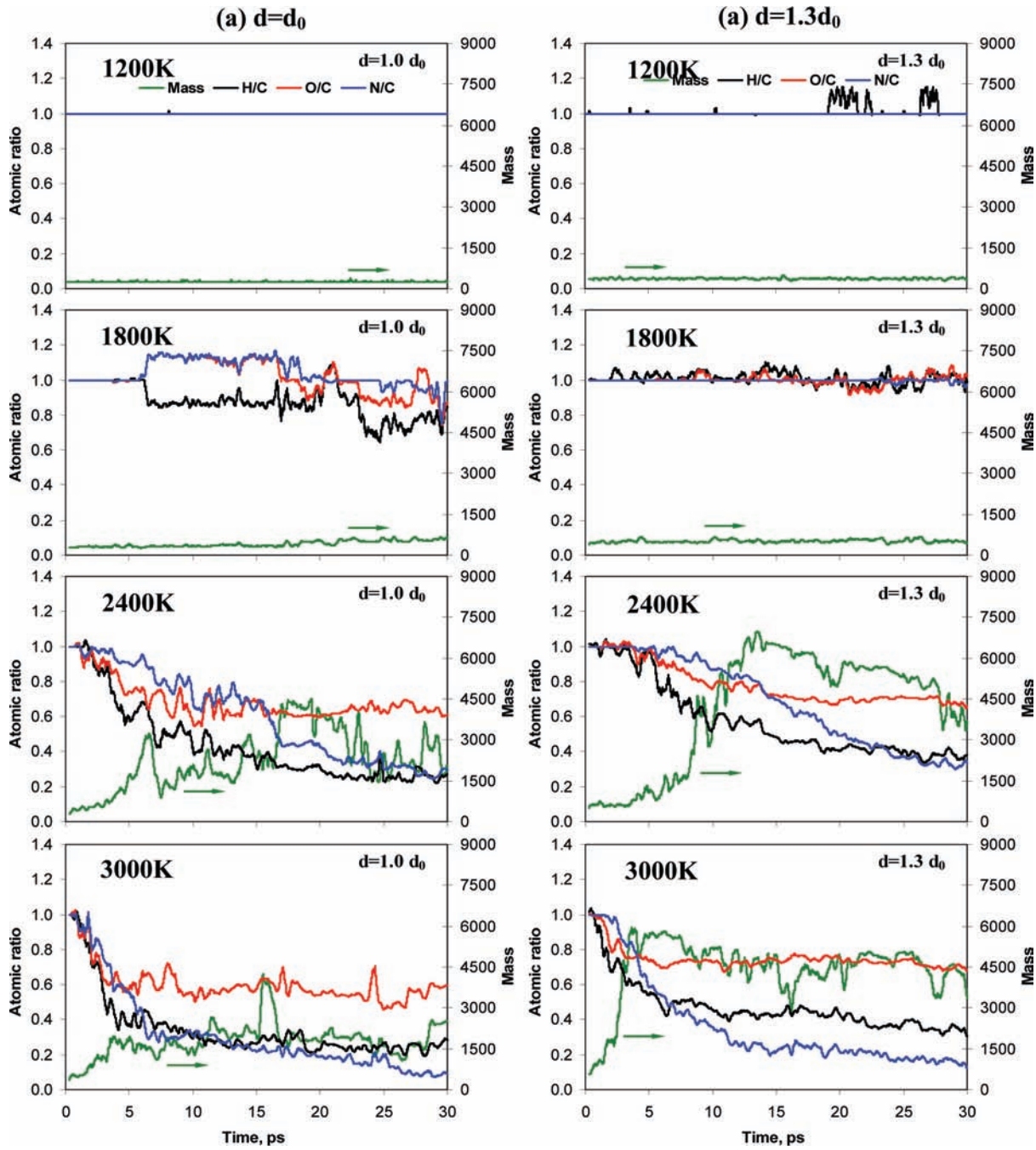

Figure 13. Fluctuations in the elemental composition (H:C, black line; O:C, red line; N:C, blue line) and molecular mass (green line) during formation of the largest carbon cluster in TATB for various temperatures and densities: (a) $d_0 = 1.88$ g/cm^3 and (b) $1.3d_0 = 2.44$ g/cm^3.

reasonably stable under these conditions, dropping in size by only 20−40% after the initial formation on the 30-ps simulation time scale.

There are no direct experimental measurements of the carbon clustering kinetics in the reaction zone of the detonation wave. The continuum simulation models employ theoretical estimates that assume carbon cluster formation from the gaseous detonation products and atomic carbon.[31,32] However, our results show that the formation of carbonaceous clusters begins before complete decomposition of TATB molecules into the secondary products (water, nitrogen, carbon oxides, and others). Then we find that these clusters slowly release oxygen and nitrogen, producing additional secondary products while transforming into clusters with increased carbon content. The condensed-phase kinetics of energy-releasing reactions in carbon-rich explosives can be substantially affected by the cluster formation process, which involves three major stages:

(i) Initial agglomeration of carbonaceous intermediates obtained after primary (endothermic) decomposition reactions that eliminate water and other small-weight intermediate products, such as NO and NO_2;

(ii) dissociation of noncarbon atoms from these aggregates during secondary reactions and coalescence of nanocarbon ribbons, rings, and sheets into carbon-rich clusters; and

(iii) coagulation of these clusters into bigger carbon spherules and crystalline grains.

On the 30-ps time scale of our simulations, we observed only the first stage and the beginning of the second stage.

A detailed analysis of the evolution of carbon-rich aggregates is presented in Figure 13a and b, which gives the elemental

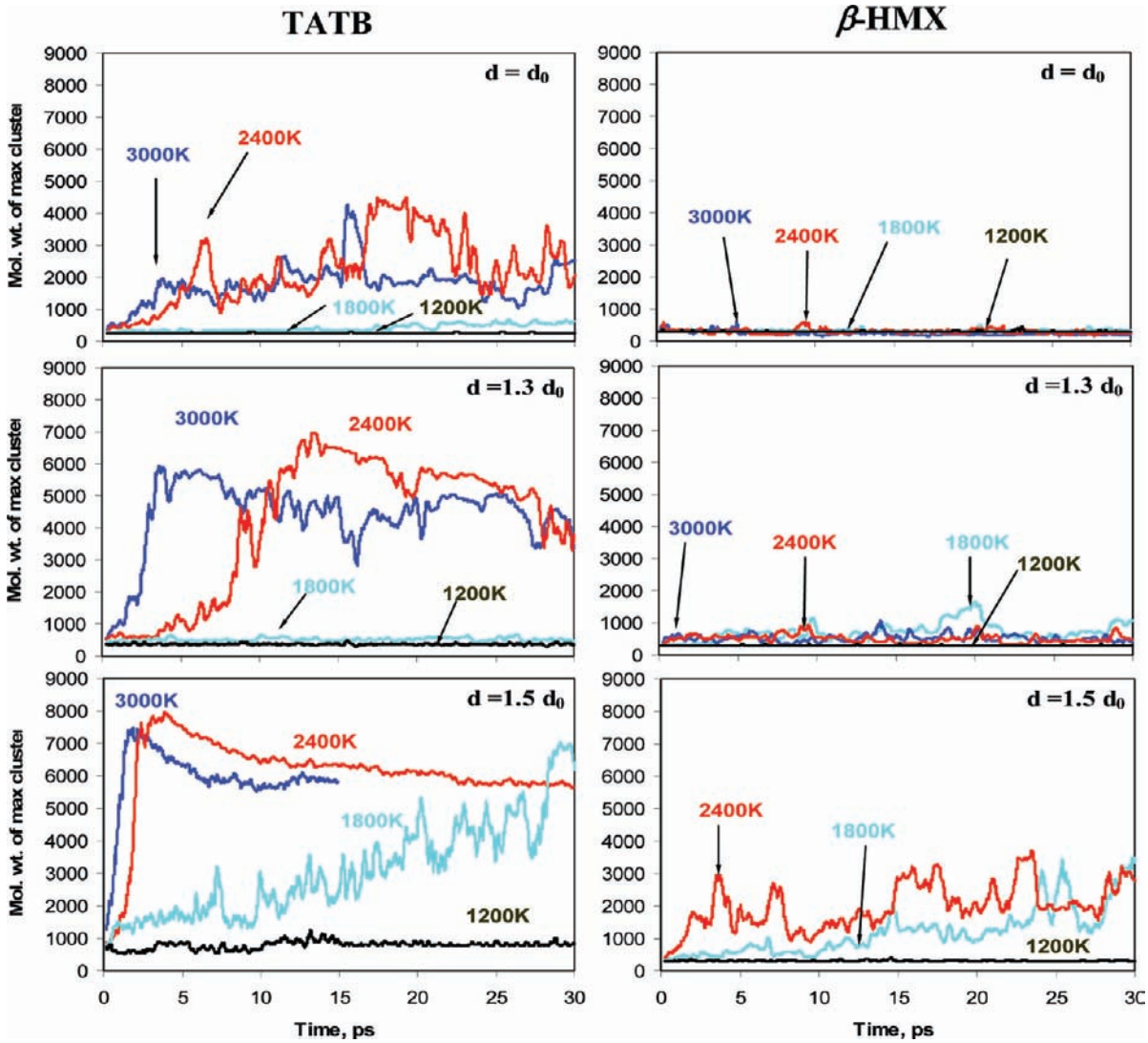

Figure 14. Time evolution of a weight of largest carbon clusters formed in TATB (left column) and HMX (right column) for densities d_0, $1.3d_0$, and $1.3d_0$ ($d_{0,\mathrm{TATB}} = 1.88$ g/cm^3 and $d_{0,\beta\text{-HMX}} = 1.77$ g/cm^3) and temperatures from 1200 to 3000 K. Molecular weights of single TATB and HMX molecules are 258 and 296 amu, respectively.

composition (shown as ratios to C) of the maximum clusters in TATB at densities d_0 and $1.3d_0$. These element ratios show that the clusters slowly lose a large number of the hydrogen and nitrogen atoms (up to ~70−90% of the initial amount) during the simulations at 2400 and 3000 K.

In contrast, more than 60% of the oxygen atoms remain trapped inside the aggregate, which is considerably higher than that in the case of HMX decomposition (see Figure 7). Such "oxygen trapping" prevents its participation in the secondary reactions and results in a significant delay in the final transformation of the aggregate into carbon soot, explaining the significant length of the TATB reaction zone observed in experiments.

The final compositions of the maximum cluster are very similar in the systems with densities d_0 and $1.3d_0$, but the mass of the cluster formed at lower density is approximately two times smaller. The temperature increase from 2400 to 3000 K has almost no effect on the final ratios of the hydrogen and oxygen atoms but leads to faster dissociation of the nitrogen atoms, which correlates well with a boost in the production of the nitrogen-containing final products, such as N_2 and NH_3, at 3000 K (see Figure 11). Thus, our ReaxFF simulations indicate that the elemental composition of the maximum cluster in TATB is affected by the temperature but with almost no density dependence.

For comparison, Figure 14 summarizes the molecular weights of the maximum clusters formed in both β-HMX and TATB crystals at three different densities and various temperatures. This demonstrates clearly the formation of much bigger carbon-rich aggregates in TATB over those in HMX. For example, the maximum cluster in TATB has gathered ~47% of the total system mass (equivalent to ~15 TATB molecules), as compared to only ~6% for HMX (~2 molecules), at the end of 30-ps simulation at density $1.3d_0$ and temperature 2400 K. Figure 15 shows a detailed view of the final system configurations obtained in TATB and HMX at 3000 K. In TATB, the maximum clusters have the composition $C_{107}H_{310}O_{64}N_{12}$ for d_0 and $C_{145}H_{44}O_{98}N_{16}$ for $1.3d_0$; in HMX, the maximum clusters are $C_6H_2O_5N_3$ for d_0 and $C_{15}H_7O_{17}N_2$ for $1.3d_0$. Figure 16 shows only atoms from those clusters in TATB to demonstrate their structure after 30 ps of NVT simulation. The backbone of these clusters consists of carbon atoms combined mostly into polyaromatic rings, giving the clusters a graphitic character.

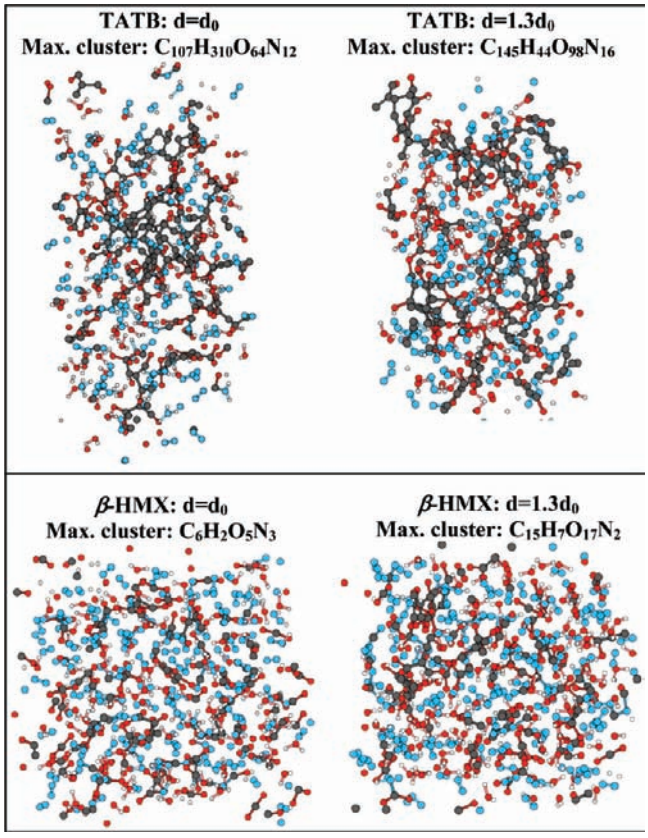

Figure 15. Snapshots of molecular configurations obtained after 30-ps MD-NVT simulations at $T = 3000$ K in TATB (top) and β-HMX (bottom) for densities d_0 and $1.3d_0$.

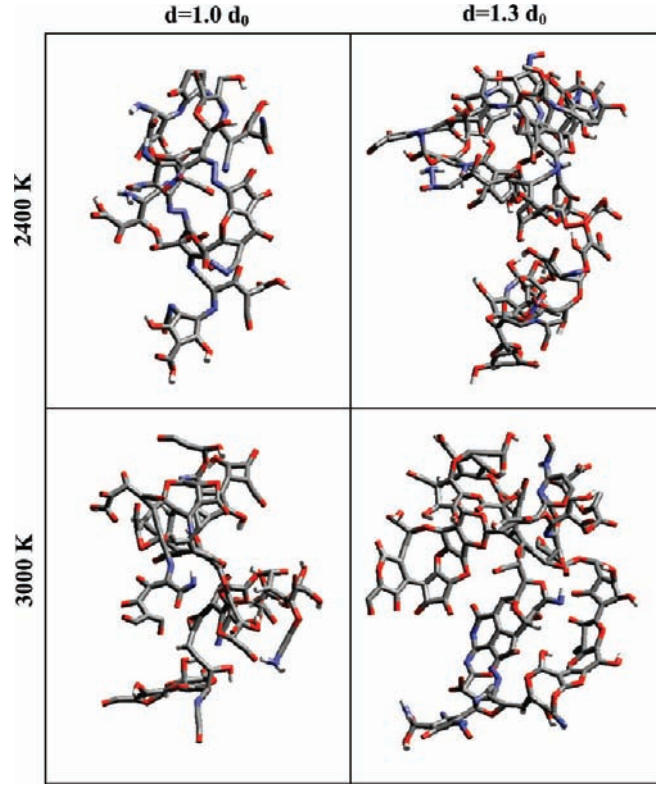

Figure 16. The final structures of the largest carbon cluster formed in TATB after 30-ps MD-NVT at temperatures $T = 2400$ K (top) and 3000 K (bottom) for densities $d_0 = 1.88$ g/cm^3 and $1.3d_0 = 2.44$ g/cm^3.

3.3. Stability of Clusters in TATB after Expansion. To study the evolution of the carbon-rich clusters after expansion of the reaction products into a free volume, we apply two procedures using variable-volume MD simulation without thermostatting:

(a) the "linear expansion" method: system volume V_0 is linearly increased (with fractional atom coordinates being scaled to the new periodic box) at each time step until it reaches $10V_0$ and

(b) the "sudden expansion" method: system volume V_0 is instantly increased to $10V_0$, and molecules/clusters split by the periodic boundaries of the initial box are unfolded in such a way that the initial atom connectivity is not altered and the atom coordinates are not scaled.

In both cases, we start from the final state of TATB system at $d = 1.0d_0$ obtained after 30-ps NVT-MD simulation at 3000 K and perform a 1.0-ps variable-volume MD simulation. For the "linear expansion" method, each cell dimension expands gradually at each time step with a rate of ~2.0 km/s. For the "sudden expansion" method, the system volume is instantly expanded to $10V_0$ (retaining the fragment connectivity) and then kept fixed during the 1.0-ps NVE-MD simulation. Application of these two methods allows us to evaluate the effect of quite different expansion rates on the cluster stability and evolution of elemental composition.

Figure 17 plots the evolution of system temperature, potential energy, and total energy from variable-volume MD simulations using these two techniques. The simulations show that many reactions occur during the first 0.2 ps as the clusters decompose, resulting in a decrease in the potential energy and an increase in the system temperature. After 0.2 ps, the fragments remain relatively stable and the system temperature stays constant in the sudden expansion simulation. Since we pump external energy into the system in the linear expansion method (because the rescaling of atom coordinates during cell expansion imposes an external stretch of ~0.002 Å/step on the each bond), the potential energy and system temperature increase continuously after ~0.15 ps, which leads to an increase in the total energy (Figure 17c). An alternative is to model expansion into a free volume using the sudden expansion technique, in which atom coordinates are not rescaled, but a surface not going through any bonds is introduced while expanding the cell. Such expansion conditions may occur in laser-induced ablation or during the passage through a void or crack.

In the absence of an open volume (the case of a detonation wave), the expansion will proceed at a rate determined by the balance between exothermic energy release and the work done by expanding gaseous products to sustain the shock compression in surrounding bulk material at the detonation front. The realistic simulation of such expansion should (1) satisfy the Rankine−Hugoniot relationships during the evolution of the system to the Chapman−Jouguet point, and (2) avoid the atom coordinates' rescaling and the use of the periodic boundary conditions during the volume change. These requirements can be satisfied in large-scale nonequilibrium MD simulation of the detonation wave propagation, but it is beyond the scope of this paper. Our study of the evolution of expanding products during either sudden or linear expansion is mainly focused on the stability of formed carbon clusters (for example, would they survive the sudden expansion of products into vacuum, etc.) and should not be directly compared to the bulk detonation conditions.

Figure 18a and b shows how the molecular weights of the five largest clusters change during simulations with both procedures. Essentially, the trends of weight evolution are very similar to each other, although the final compositions of these

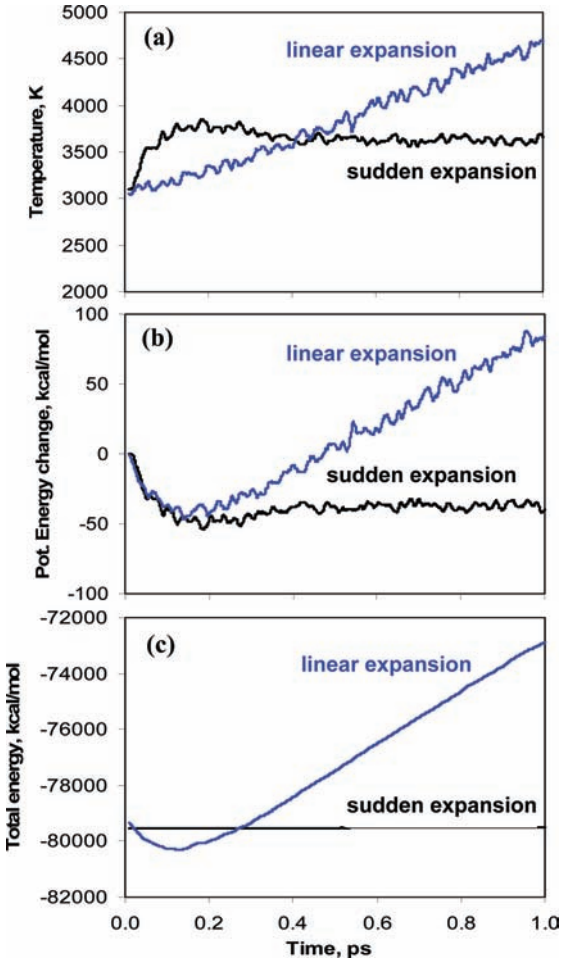

Figure 17. Evolution of (a) system temperature, (b) potential energy, and (c) total energy in TATB during MD simulations with 10-fold volume expansion by linear expansion and sudden expansion techniques. The initial configuration was taken from the last step of 30-ps NVT-MD simulation at 3000 K with density $d_0 = 1.88$ g/cm^3 and then expanded to $d = 0.188$ g/cm^3.

clusters at 1.0 ps are slightly different. For example, the maximum cluster at the end of simulation has the composition $C_{44}H_7O_{13}N_4$ for the linear expansion method and $C_{45}H_7O_{18}N_3$for the sudden expansion method. The detailed evolution of the elemental composition of the maximum cluster shown in Figure 19 indicates that it has less fluctuation in case of the sudden expansion method. The structures of the maximum cluster obtained at the beginning and at the end of the sudden expansion simulation are shown in Figure 20a and b, respectively. The final structure has a graphitic character, as evidenced by a few interlinked six-membered carbon rings.

The theoretical phase diagram for carbon clusters[31,40,41] shows that the phase boundaries between diamond, graphite, and liquid carbon depend on the differences in surface energy between the three phases and are sensitive to the cluster size. When the number of atoms in the cluster is small ($n \sim 100$), the diamond region becomes quite narrow while the graphite phase spans over a much broader range of temperatures and pressures. At the conditions of the 1.0 ps MD simulation described above ($T = 3000$ K and $P = 2.0$ GPa), the stable carbon clusters should form the graphitic phase. Therefore, the structure of the carbon clusters observed in these ReaxFF MD simulations is consistent with that suggested by the phase diagram of nanocarbon.

To explore the structure and stability of the clusters at the conditions in which they would be examined experimentally,

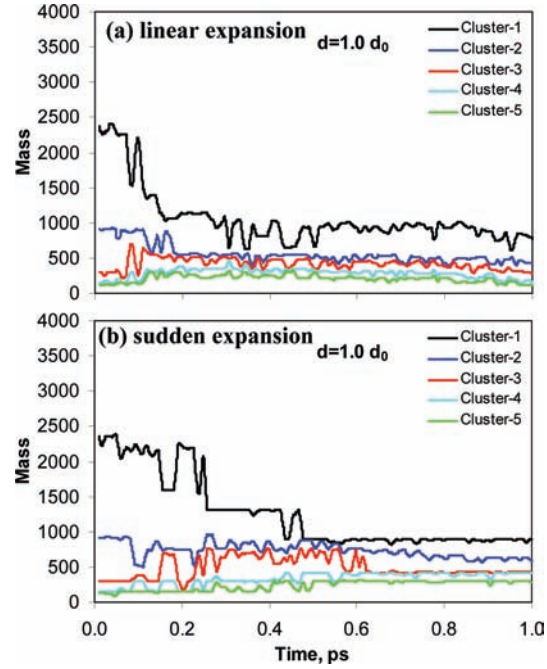

Figure 18. Time evolution of a weight of five largest clusters in TATB at $T = 3000$ K during MD simulations with 10-fold volume expansion (from density $d_0 = 1.88$ to $d = 0.188$ g/cm^3) by the (a) linear expansion and (b) sudden expansion techniques.

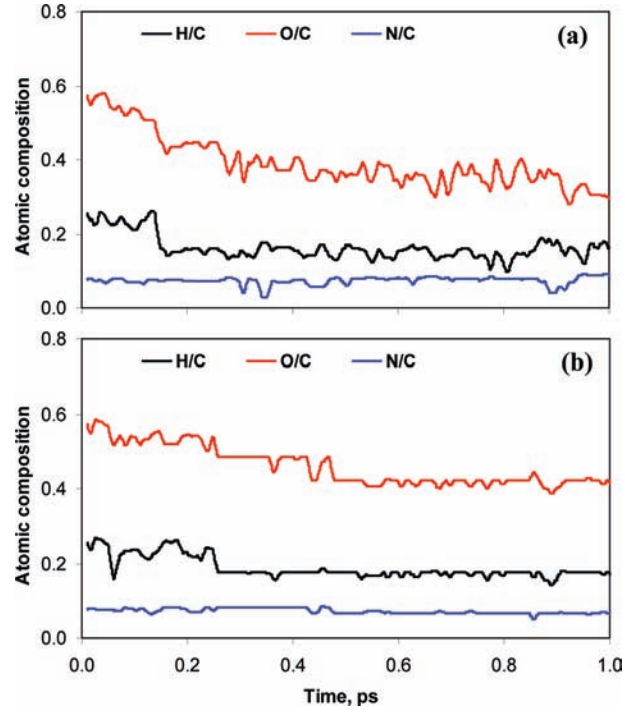

Figure 19. Fluctuations in composition of the largest carbon cluster in TATB at initial density $d_0 = 1.88$ g/cm^3 and temperature $T = 3000$ K during MD simulations with 10-fold volume expansion by the (a) linear expansion and (b) sudden expansion techniques.

we also simulated fast-cooling annealing starting from the same configuration as in the sudden expansion method (obtained by the instantaneous 10-fold expansion of the system volume). In this "sudden expansion + cooling" simulation, we cool down the system gradually from 3000 to 500 K at a rate of 100 K/ps and then keep it at a constant temperature of 500 K for another 10 ps. The evolution of molecular weights of the five largest clusters plotted in Figure 21 shows that the fast-cooling

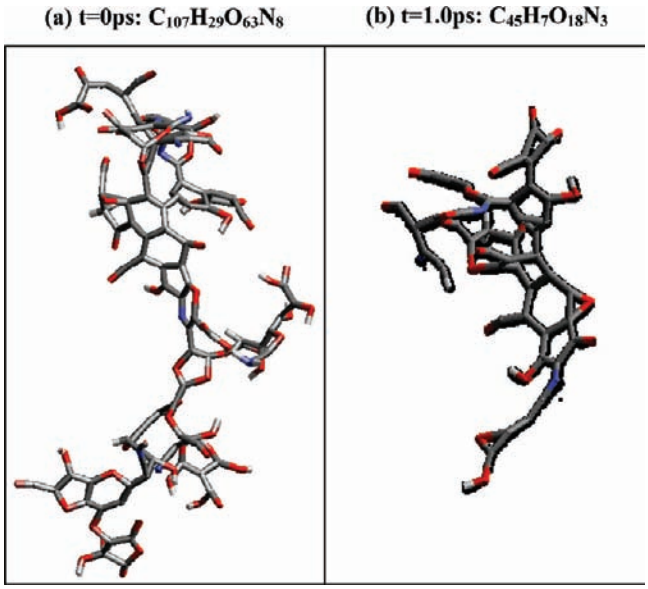

Figure 20. Snapshots of (a) initial and (b) final structures of the largest carbon cluster in TATB at $d_0 = 1.88$ g/cm^3 and $T = 3000$ K observed in 1-ps MD simulation with sudden expansion of the volume from V_0 to $10V_0$.

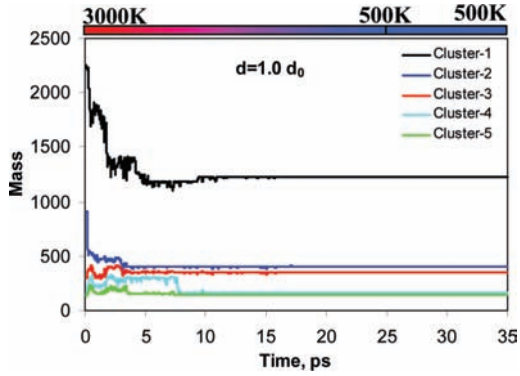

Figure 21. Evolution of the molecular weight of the five largest clusters in 10-fold expanded TATB ($d = 0.188$ g/cm^3) during a 35-ps cooldown from $T = 3000$ to 500 K. The initial configuration was taken from the last step of the sudden expansion simulation.

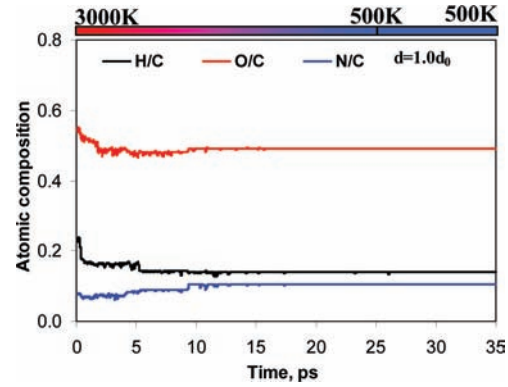

Figure 22. Fluctuations in composition of the largest carbon cluster in 10-fold expanded TATB ($d = 0.188$ g/cm^3) during a 35-ps cooldown from $T = 3000$ to 500 K. The initial configuration was taken from the last step of the sudden expansion simulation.

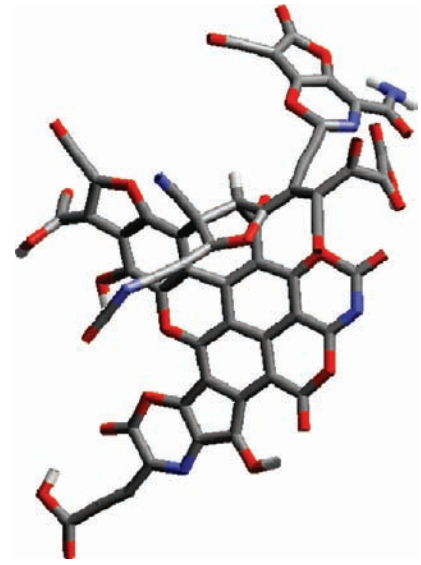

Figure 23. Final structure of the largest carbon cluster formed in 10-fold expanded TATB ($d = 0.188$ g/cm^3) after cooling down from $T = 3000$ to 500 K. The configuration was taken from the last step of the sudden expansion simulation.

annealing produces larger and more stable clusters than those formed in the "sudden expansion + NVE" simulation. The weight of the maximum cluster obtained after 35 ps of annealing down to 500 K is about 1250 amu, as compared to ~880 amu in the sudden expansion with NVE simulation at a final temperature of ~3600 K. As shown by Figure 22, the maximum cluster changes its composition from $C_{107}H_{29}O_{63}N_8$ to $C_{57}H_8O_{28}N_6$ during the first 10 ps of the simulated cooling from 3000 to ~2000 K and does not change at all thereafter for next 15 ps of cooling down to 500 K. The final structure of the maximum cluster after 25 ps of cooling and 10 ps of NVT-MD at 500 K displayed in Figure 23 exhibits a graphitic character with insertions of oxygen atoms.

We also performed a NVT-MD simulation for a larger TATB crystallite at 3000 K to check the size effect on the formation of carbon-rich clusters. The TATB system used in the previous simulations was duplicated by ($2 \times 2 \times 1$) to create a $4 \times 4 \times 4$ supercell with 128 molecules. Figure 24a shows the molecular weights of the five largest clusters formed in the previous 32-TATB molecule systems; Figure 24b shows the same for the expanded 128-molecule TATB system, both with density d_0 for 30 ps of simulation at 3000 K. The maximum cluster in the 128-molecule system has the composition $C_{215}H_{58}O_{110}N_{32}$ and a weight of 4846 amu (~15% of the total system mass) at the end of the simulation, which compares to 2433 amu (~30% of the total system mass) for the maximum cluster $C_{107}H_{29}O_{63}N_8$ in the 32-molecule system. The other four largest clusters have gathered ~16% of the total mass in the 128-molecule system and ~18% in the 32-molecule system. Their compositions are $C_{90}H_{28}O_{54}N_9$, $C_{69}H_{12}O_{39}N_9$, $C_{34}H_{13}O_{22}N_6$, and $C_{34}H_5O_{21}N_2$ for the 128-molecule system and $C_{37}H_9O_{27}N_3$, $C_{12}H_2O_{10}$, $C_5H_3O_3N_3$, and $C_5HO_2N_2$ for the 32-molecule system. The detailed evolution of the elemental composition of the maximum cluster during MD simulation in the 128-molecule system is shown in Figure 25. The variation of the ratios of H, O, and N atoms to C atoms is much the same as for the smaller system (see Figure 13). The final compositions of the maximum clusters in both large and small systems are quite similar and contain a significantly smaller number of nitrogen and hydrogen atoms than oxygen atoms. Figure 26 illustrates the final structure of the maximum cluster formed in the 128-molecule TATB system after 30 ps of simulation at 3000 K. Thus, the 4-times-larger TATB system leads to carbon-rich clusters that are about twice as big as for the smaller system.

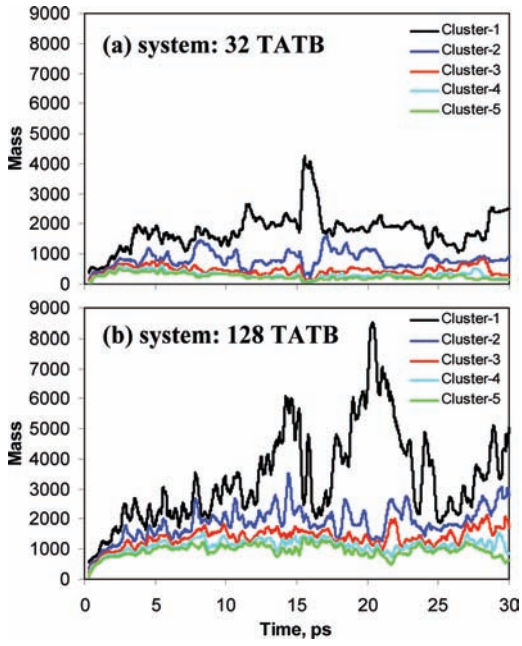

Figure 24. Molecular weight of five largest clusters formed in TATB with density $d_0 = 1.88$ g/cm^3 during 30-ps MD-NVT at $T = 3000$ K in a supercell containing (a) 32 TATB and (b) 128 TATB molecules.

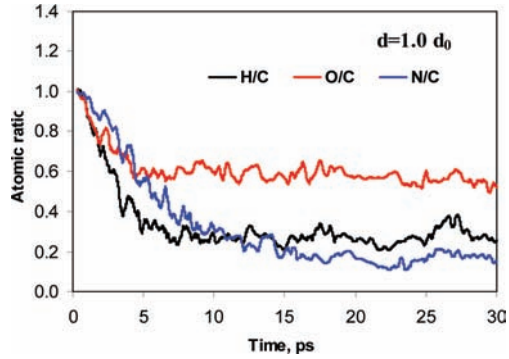

Figure 25. Fluctuations in elemental composition of the largest cluster formed in a TATB supercell with 128 molecules during MD-NVT at $T = 3000$ K for density $d_0 = 1.88$ g/cm^3.

These results are in agreement with detonation experiments, which observed the formation of ultrafine diamonds, graphite, and amorphous carbon in postdetonation soot from TNT, TNT/RDX, TNT/HMX, TNT/TATB, and other pure and composite explosives.[18−27]

4. Summary

We report here MD simulations using the first-principles-based ReaxFF reactive force field to study the thermal decomposition of β-HMX and TATB crystals at several temperatures (1200−3000 K) and densities (d_0 to $1.5d_0$, where d_0 is the zero-pressure density). Our simulations demonstrate formation of sizable carbonaceous clusters with graphitic structure in TATB, but not in HMX.

At the lowest temperature of 1200 K, we find no cluster formation in either TATB or β-HMX during the 30 ps of the simulation at any density. At 1800 K, we observe a few small and very unstable aggregates formed in HMX at 30% elevated density, but none in TATB. In fact, TATB exhibits very little reactivity at this temperature, resulting mainly in the formation of a few water molecules. We find negligibly small amounts of

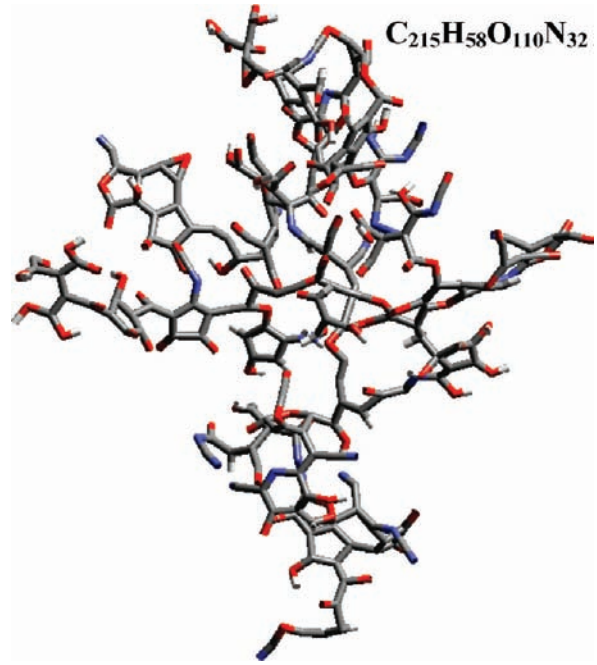

Figure 26. Final structure of the largest carbon cluster formed in a supercell with 128 TATB molecules after 30-ps MD-NVT at $T = 3000$K for density $d_0 = 1.88$ g/cm^3.

NO_2 and HONO products from TATB at 1800 K, suggesting that C−NO_2 bond cleavage is not the primary mechanism responsible for the initiation of TATB dissociation at temperatures below ∼2000 K.

In contrast, at temperatures of 2400 and 3000 K and at all densities, we observed formation of large carbon-rich aggregates in TATB. Indeed, the maximum molecular weight of TATB clusters is much larger than that obtained from HMX, despite the total number of decomposition fragments in TATB being considerably lower than in HMX. The size of the largest cluster in TATB increases significantly with increased density. At higher temperature, the largest clusters form earlier, but they also react more readily in secondary processes to produce the final gaseous products.

We find that the carbonaceous clusters formed in the decomposition of TATB capture significant amounts of oxygen, (O:C ∼ 0.6−0.7 at temperatures of 2400 and 3000 K), preventing its participation in the secondary reactions. In contrast, both H:C and N:C quickly decrease to 0.4−0.3 and 0.3−0.1, depending on the temperature and density. This trapping of oxygen (and to a lesser extent, nitrogen and hydrogen) inside the cluster should have a serious impact on the reaction kinetics, leading eventually to a significant expansion of the reaction zone. The process of releasing hydrogen, nitrogen, and oxygen from the cluster would eventually produce relatively pure carbon soot. Such simulation data should be useful in developing quantitative models of the reaction processes in TATB, which are not well explained in current thermochemical approaches.

On the basis of the ReaxFF MD simulations, we extracted chemical kinetic rates for the decomposition of HMX and TATB that can be compared to overall rates deduced from experiment. For the primary step involving overall endothermic processes, the rate for HMX is about an order of magnitude faster than for TATB, but in both cases, the rate is much slower (by 1−4 orders, depending on temperature and model) than those in the Rogers and Tarver models. For the second step involving initial

reactions of the decomposition products, the rates for HMX and TATB are comparable at high temperatures (2400−3000 K), but TATB forms large carbonaceous clusters that continue to transform slowly into solid carbon and gases on a time scale beyond our simulation limit.

Summarizing, our ReaxFF MD simulations of condensed-phase thermal decomposition of TATB and HMX yield the following results:

(1) Carbonaceous clusters formed in TATB are much larger and more stable than those obtained from HMX (the largest cluster in HMX gather the mass of only ∼2−3 molecules, as compared to ∼10−15 molecules for TATB);

(2) the formation of clusters begins shortly after the primary endothermic reactions that eliminate small intermediates and products such as NO, OH, NO_2, and H_2O (i.e., without complete decomposition as in the gas phase) and involves agglomeration of radicals and large intermediates, such as partially dissociated molecules, and, in the case of TATB, carbon rings;

(3) as a result of incomplete decomposition, a large number of noncarbon atoms remain trapped inside the cluster, delaying secondary reactions and further transformation of the cluster into carbon soot;

(4) in TATB, oxygen atoms are usually trapped in the cluster (bonded to C) during the growth, suppressing formation of CO and CO_2, while most of the nitrogen and hydrogen atoms outgas rapidly in the form of nitrogen-containing molecules, such as N_2 and NH_3.

(5) In contrast, for HMX, the concentration of oxygen in clusters decreases faster than that of nitrogen, promoting its participation in secondary reactions and condensed-phase formation of noticeable amount of CO_2;

(6) the initial steps of HMX decomposition in the condensed phase involve homolytic cleavage of the NNO_2 bond, with formation of NO_2 and, to a lesser extent, HONO;

(7) the initial steps of TATB decomposition in the condensed phase at low temperature leads to the formation of H_2O molecules without cleavage of the $C-NO_2$ bond. However, a small amount of NO_2 and HONO is detected at higher temperature, indicating the existence of an alternative pathway for decomposition at high temperatures;

(8) at high density ($1.3d_0$ and $1.5d_0$), TATB molecules exhibit dimerization reactions, providing an alternative endothermic pathway for the absorption of external energy. This might play a role in reducing the sensitivity of the TATB crystals under shock compression.

Our analysis of the structure of the carbon-rich clusters formed in TATB shows that they contain polyaromatic rings and graphitic regions. We did not observe the tetrahedral bonding in these clusters that would be expected to lead to production of diamondoids. This may be because diamond formation processes require much larger system sizes for much longer times to form stable clusters, as compared to graphitic regions.

5. Conclusion

These studies show that ReaxFF MD provides detailed atomistic information that helps to explain such macroscopic observations as the dramatic difference in carbon cluster formation between TATB and HMX. This shows that ReaxFF MD captures the fundamental differences in the mechanisms of such systems and illustrates how ReaxFF may be applied to complex chemical phenomena. The studies here include only modestly sized systems and modest periods; however, ReaxFF calculations of reactive processes have already been reported on systems with a few millions of atoms.[42,43] Thus, with suitable high-performance parallel computers, one can consider studies of chemical processes at the atomistic level for complex systems under extreme conditions.

Acknowledgment. This research was supported by the Office of Naval Research (Grant no. N00014-05-1-0778 and N00014-09-1-0634, program managers Dr. Judah Goldwasser and Cliff Bedford), the Army Research Office (MURI Grant no. W911NF-05-1-0345, program managers Dr. David Mann and Dr. Ralph Anthenien), and the U.S. Department of Energy (65287-001-08 through Los Alamos National Laboratory). The computer facilities were provided by ONR-DURIP and ARO−DURIP.

Supporting Information Available: Additional information as noted in text. This material is available free of charge via the Internet at http://pubs.acs.org.

References and Notes

(1) van Duin, A. C. T.; Dasgupta, S.; Lorant, F.; Goddard, W. A. *J. Phys. Chem. A* **2001**, *105*, 9396.
(2) Strachan, A.; van Duin, A. C. T.; Chakraborty, D.; Dasgupta, S.; Goddard, W. A. *Phys. Rev. Lett.* **2003**, *91*, 09301.
(3) Strachan, A.; Kober, E.; van Duin, A. C. T.; Oxgaard, J.; Goddard, W. A. *J. Chem. Phys.* **2005**, *122*, 054502.
(4) van Duin, A. C. T.; Zeiri, Y.; Dubnikova, Y. F.; Kosloff, R.; Goddard, W. A. *J. Am. Chem. Soc.* **2005**, *127*, 11053.
(5) Chenoweth, K.; Cheung, S.; van Duin, A. C. T.; Goddard, W. A.; Kober, E. M. *J. Am. Chem. Soc.* **2005**, *127*, 7192.
(6) Zhang, Q.; Cagin, T.; van Duin, A. C. T.; Goddard, W. A.; Qi, Y.; Hector, L. *Phys. Rev. B* **2004**, *69*, 045423.
(7) Nielson, K.; van Duin, A. C. T.; Oxgaard, J.; Deng, W.; Goddard, W. A. *J. Phys. Chem. A* **2005**, *109*, 493.
(8) Cheung, S.; Deng, W.; van Duin, A. C. T.; Goddard, W. A. *J. Phys. Chem. A* **2005**, *109*, 851.
(9) van Duin, A. C. T.; Strachan, A.; Stewman, S.; Zhang, Q.; Xu, X.; Goddard, W. A. *J. Phys. Chem. A* **2003**, *107*, 3803.
(10) Buehler, M. J.; van Duin, A. C. T.; Goddard, W. A. *Phys. Rev. Lett.* **2006**, *96*, 095505.
(11) Ludwig, J.; Vlachos, D. G.; van Duin, A. C. T.; Goddard, W. A. *J. Phys. Chem. B* **2006**, *110*, 4274.
(12) Goddard, W. A.; van Duin, A. C. T.; Chenoweth, K.; Cheng, M. J.; Pudar, S.; Oxgaard, J.; Merinov, B.; Jang, Y. H.; Persson, P. *Top. Catal.* **2006**, *38*, 93.
(13) Goddard, W. A.; Merinov, B.; van Duin, A. C. T.; Jacob, T.; Blanco, M.; Molinero, V.; Jang, S. S.; Jang, Y. H. *Mol. Simul.* **2006**, *32*, 251.
(14) Shenderova, O. A.; Zhirnov, V. V.; Brenner, D. W. *Crit. Rev. Solid State Mater. Sci.* **2002**, *27*, 227.
(15) Danilenko, V. V. *Phys. Solid State* **2004**, *46*, 595.
(16) Volkov, K. V.; Danilenko, V. V.; Elin, V. I. *Combust. Explos. Shock Waves* **1990**, *26*, 366.
(17) Staver, A. M.; Gubareva, N. V.; Lyamkin, A. I.; Petrov, E. A. *Combust. Explos. Shock Waves* **1984**, *20*, 567.
(18) Greiner, N. R.; Phillips, D. S.; Johnson, J. D.; Volk, F. *Nature* **1988**, *333*, 440.
(19) Danilenko, V. V. *Synthesis and Sintering of Diamond by Explosion*; Energoatomizdat: Moscow, 2003.
(20) Yamada, K.; Sawaoka, A. B. *Carbon* **1994**, *32*, 665.
(21) Mironov, E. V.; Petrov, E. A.; Korets, A. Y. *Combust. Explos. Shock Waves* **2004**, *40*, 473.
(22) Chen, P.; Huang, F.; Yun, S. *Carbon* **2003**, *41*, 2093.
(23) Anisichkin, V. F.; Dolgushin, D. S.; Petrov, E. A. *Combust. Explos. Shock Waves* **1995**, *31*, 106.
(24) Titov, V. M.; Anisichkin, V. F.; Mal'kov, I. Y. *Combust. Explos. Shock Waves* **1989**, *25*, 372.
(25) Kruger, A.; Kataoka, F.; Ozawa, M.; Fujino, T.; Suzuki, Y.; Aleksenski, A. E.; Vul, A. Y.; Osawa, E. *Carbon* **2005**, *43*, 1722.
(26) Mal'kov, I. Y.; Filatov, L. I.; Titov, V. M.; Litvinov, B. V.; Chuvilin, A. L.; Teslenko, T. S. *Combust. Explos. Shock Waves* **1994**, *29*, 542.
(27) Xu, T.; Xu, K.; Zhao, J. *Mater. Sci. Eng., B* **1996**, *38*, L1–L4.
(28) Anisichkin, V. F. *Combust. Explos. Shock Waves* **1994**, *30*, 667.
(29) Shaw, M. S.; Johnson, J. D. *J. Appl. Phys.* **1987**, *62*, 2080.
(30) van Thiel, M.; Ree, F. H. *J. Appl. Phys.* **1987**, *62*, 1761.
(31) Viecelli, J. A.; Ree, F. H. *J. Appl. Phys.* **2000**, *88*, 683.
(32) Viecelli, J. A.; Bastea, S.; Glosli, J. N.; Ree, F. H. *J. Chem. Phys.* **2001**, *115*, 2730.

(33) Chakraborty, D.; Muller, R. P.; Dasgupta, S.; Goddard, W. A. *J. Comp.-Aided Mater. Des.* **2002**, *8*, 203.
(34) Chakraborty, D.; Muller, R. P.; Dasgupta, S.; Goddard, W. A. *J. Phys. Chem. A* **2001**, *105*, 1302.
(35) Lewis, J. P.; Glaesemann, K. R.; van Opdrop, K.; Voth, G. A. *J. Phys. Chem. A* **2000**, *104*, 11384.
(36) Behrens, R., Jr. *J. Phys. Chem.* **1990**, *94*, 6706.
(37) Manaa, M. R.; Fried, L. E.; Melius, C. F.; Elstner, M.; Frauenheim, Th. *J. Phys. Chem. A* **2002**, *106*, 9024.
(38) Quenneville, J. Private communication.
(39) Wu, C. J.; Fried, L. E. *J. Phys. Chem. A* **2000**, *105*, 1302.
(40) Vereshchagin, A. L.*Combust. Explos. Shock Waves* **2002**, *38*, 358.
(41) Danilenko, V. V.*Combust. Explos. Shock Waves* **2005**, *41*, 460.
(42) Nomura, K.; Kalia, R. K.; Nakano, A.; Vashishta, P.; van Duin, A. C. T.; Goddard, W. A. *Phys. Rev. Lett.* **2007**, *99*, 148303.
(43) Nakano, A.; Kalia, R. K.; Nomura, K.; Sharma, A.; Vashishta, P.; Shimojo, F.; van Duin, A. C. T.; Goddard, W. A.; Biswas, R.; Srivastava, D. *Comput. Mater. Sci.* **2006**, *48*, 642.
(44) Mortier, W. J.; Ghosh, S. K.; Shankar, S. *J. Am. Chem. Soc.* **1986**, *108*, 4315.
(45) Smirnov, K. S.; van de Graaf, B. *J. Chem. Soc., Faraday Trans.* **1996**, *92*, 2469.
(46) Rappe, A. K.; Goddard, W. A. *J. Phys. Chem.* **1991**, *95*, 3358.
(47) Loboiko, B. G.; Lubyatinsky, S. N. *Combust. Explos. Shock Waves* **2000**, *36*, 716.
(48) Sheffield, S. A.; Bloomquist, D. D.; Tarver, C. M. *J. Chem. Phys.* **1984**, *80*, 3831.
(49) Henson, B. F.; Smilowitz, L.; Asay, B. W.; Dickson, P. M.; Howe, P. M. *12th Symposium (International) on Detonation; ONR 333-05-2*, 2002; p 987.
(50) Henson, B. F.; Smilowitz, L.; Asay, B. W.; Sandstrom, M. M.; Romero, J. J. *13th Symposium (International) on Detonation; ONR 351-07-01*, 2006; p 778.
(51) Henson, B. F.; Smilowitz, L.; Romero, J.; Asay, B. W.; Dickson, P. M. *Shock Compression of Condensed Matter−2005*; Proceedings of the Conference of the American Physical Society Topical Group on Shock Compression of Condensed Matter, Baltimore, Maryland, July 31−August 5, 2005 ; Furnish, M. D., Elert, M., Russel, T. P., White, C. T., Eds.; AIP: Melville, N.Y., 2006; Vol. 845, p 1077.
(52) Menikoff, R. *Combust. Theory Model.* **2007**, *12*, 73–91.
(53) McGuire, R. R.; Tarver, C. M. *Seventh Symposium (International) on Detonation*; Naval Surface Weapons Center NSWC MP 82-334, Annapolis, MD, 1981, p 56.
(54) Tarver, C. M.; Chidester, S. K.; Nichols, A. L. *J. Phys. Chem.* **1996**, *100*, 5794.
(55) Tarver, C. M.; Tran, T. D. *Combust. Flame* **2004**, *137*, 50.
(56) Gibbs, T. R., Popolato, A., Eds.; *LASL Explosive Property Data*; University of California Press: Berkeley, CA, 1980.
(57) Ornellas, D. L. *Calorimetric Determinations of the Heat and Products of Detonation for Explosives*; Report UCRL-52821: October 1961 to April 1982; Lawrence Livermore National Laboratory; **1982**.
(58) Ornellas, D. L. *J. Phys. Chem.* **1968**, *72*, 2390.
(59) Manaa, M. R.; Fried, L. E. Unpublished results.
(60) Ree, F. H.; Pitz, W. J.; van Thiel, M.; Souers, P. C. *J. Phys. Chem.* **1996**, *100*, 5761.

JP901353A